

12

DNA 3903F

FRAGMENTATION PROCESSES IN SOFT ROCK

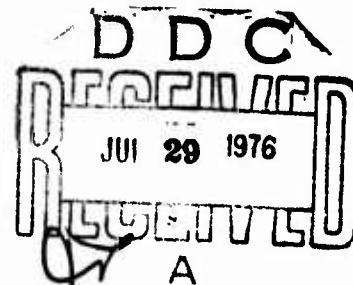
University of California
Berkeley Campus, Room 8
2543 Channing Way
Berkeley, California 94720

1 January 1976

Final Report for Period 15 May 1973—30 November 1975

CONTRACT No. DNA 001-73-C-0226

APPROVED FOR PUBLIC RELEASE;
DISTRIBUTION UNLIMITED.



THIS WORK SPONSORED BY THE DEFENSE NUCLEAR AGENCY
UNDER RDT&E RMSS CODE B344074464 Y99QAXSA00142 H2590D.

Prepared for

Director

DEFENSE NUCLEAR AGENCY

Washington, D. C. 20305

AD A 027502

Destroy this report when it is no longer
needed. Do not return to sender.

UNCLASSIFIED

SECURITY CLASSIFICATION OF THIS PAGE (When Data Entered)

REPORT DOCUMENTATION PAGE		READ INSTRUCTIONS BEFORE COMPLETING FORM
1. REPORT NUMBER DNA 3903F	2. GOVT ACCESSION NO.	3. RECIPIENT'S CATALOG NUMBER
4. TITLE (and Subtitle) FRAGMENTATION PROCESSES IN SOFT ROCK.	5. TYPE OF REPORT & PERIOD COVERED Final Report for Period 15 May 73-30 Nov 75	6. PERFORMING ORG. REPORT NUMBER
7. AUTHOR(s) Werner/Goldsmith Jerome L. Sackman	8. CONTRACT OR GRANT NUMBER(s) DNA 001-73-C-0226	
9. PERFORMING ORGANIZATION NAME AND ADDRESS University of California Berkeley Campus, Room 8 2543 Channing Way, Berkeley, California 94720	10. PROGRAM ELEMENT, PROJECT, TASK AREA & WORK UNIT NUMBERS DNA NWED-Subtask QAXSA001-42	
11. CONTROLLING OFFICE NAME AND ADDRESS Director Defense Nuclear Agency Washington, D.C. 20305	12. REPORT DATE 1 January 1976	
14. MONITORING AGENCY NAME & ADDRESS (if different from Controlling Office)	13. NUMBER OF PAGES 96	
	15. SECURITY CLASS (of this report) UNCLASSIFIED	
	15a. DECLASSIFICATION/DOWNGRADING SCHEDULE	
16. DISTRIBUTION STATEMENT (of this Report) Approved for public release; distribution unlimited.		
17. DISTRIBUTION STATEMENT (of the abstract entered in Block 20, if different from Report)		
18. SUPPLEMENTARY NOTES This work sponsored by the Defense Nuclear Agency under RDT&E RMSS Code B344074464 Y99QAXSA00142 H2590D.		
19. KEY WORDS (Continue on reverse side if necessary and identify by block number) Fracture of Rock Cratering Ejecta Waves in Rock Rock Fragmentation Comminution of Rock Rock Penetration Compaction of Rock Impact on Rocks		
20. ABSTRACT (Continue on reverse side if necessary and identify by block number) An experimental investigation has been undertaken to study the fragmentation of soft and hard rock under conditions of impact by spherical steel projectiles and standard ammunition. Laboratory tests involving the firing of 1/4-inch-diameter steel spheres have been conducted both on the Berkeley campus and at the Naval Weapons Center, China Lake. The velocity range at the first site was from 150 to about 1000 ft/sec, using a compressed gas gun, whereas that at the second location using a powder gun		

DD FORM 1 JAN 73 1473

EDITION OF 1 NOV 65 IS OBSOLETE

UNCLASSIFIED

SECURITY CLASSIFICATION OF THIS PAGE (When Data Entered)

071 850

mt

UNCLASSIFIED

SECURITY CLASSIFICATION OF THIS PAGE(When Data Entered)

20. ABSTRACT (Continued)

for the sphere ranged from 1100 to 8500 ft/sec. The results of the first year of investigation, comprising all the work performed at China Lake, have been documented in Report DNA 3416Z; in addition, the China Lake performance was published in a separate report NWC TP 5700 (January 1975).

The present report concentrates on the activity of the second year of operation. Tests were performed to separately measure the energy contained in the waves generated by the impact in the sample, and special procedures were developed and executed to attempt to determine the surface area associated with cracks produced as the result of the collision. These tests were performed on diorite rather than on shale, since the ejecta formation in the latter was found to be negligible for the range of laboratory impact velocities utilized. Photographic measurements of the ejecta and the determination of the crater topography were continued as in the earlier tests, but the use of the ballistic pendulum and the scheme for the evaluation of the spatial distribution of the ejecta were abandoned. Tests on shale were conducted to determine the energy required for given depths of penetration.

It was found that, over a range of six decades of energy of the striker, the penetration depth in shale scaled reasonably well with both initial momentum and initial energy, and that the phenomenon could be satisfactorily modeled by a purely viscous target material that neglects elastic effects. The energy of comminution for the harder rock diorite, consisting of the difference between initial striker energy and the measured terminal energies due to waves in the target, rebound of the projectile and ejecta emission were found to be of the order of 70 to 85 percent. In view of the extreme uncertainties as to what cracks in the specimen preexisted and what fissures were directly attributable to the impact, it was only possible to give bounds for the energy required to produce unit new surface in the phenomenon. While the ejecta surface area was determined from the measured size distributions and a geometric configuration governed by a single linear dimension, a complete analytical representation of the comminution and ejection process will require considerable further study and experimentation.

ACCESSION for

NTIS	WFO Section	<input checked="" type="checkbox"/>
000	Dist. Section	<input type="checkbox"/>
UNCLASSIFIED		<input type="checkbox"/>
DECLASSIFIED		<input type="checkbox"/>

BY _____

DATE _____

REASON _____

APPROVED _____

REVIEWED _____

RECEIVED _____

FILED _____

SEARCHED _____

SERIALIZED _____

INDEXED _____

ADDITIONAL _____

REMARKS _____

1

UNCLASSIFIED

SECURITY CLASSIFICATION OF THIS PAGE(When Data Entered)

TABLE OF CONTENTS

	<u>Page</u>
Section I Introduction	5
Section II Summary of First Year Activity	7
Section III Liaison with Stanford Research Institute	14
Section IV Work performed during the Second Contract Year	14
IV.A Sample Preparation	15
IV.B Experimental Apparatus and Procedure	23
IV.C Results and Discussion	33
1. Diorite	33
a. Velocity Measurements	33
b. Ejecta	36
c. Wave Energy	53
d. Crater	56
e. Cracks	56
f. Relation of Results to Comminution Theories	69
2. Shale	72
a. Ejecta	72
b. Dynamic Penetration	74
c. Quasi-static Tests	77
d. Correlation of Penetration Data	81
Section V Summary	84
List of References	87
Appendix A Computer Program for Crack Surface Area Evaluation	89

LIST OF ILLUSTRATIONS

<u>Figure</u>	<u>Title</u>	<u>Page</u>
1	Composite Specimen with Embedded Gages	18
2	Assembly of Composite Diorite Sample	20
3	Schematic of Experimental Arrangement	24
4	Photograph of Experimental Arrangement	25
5	Typical Record of an Initial Velocity Measurement	27
6	Strain Gage Histories for Run D180	32
7a	Montage of Typical Cross-section of Diorite Sample after Impact	34
7b	Sectioning Scheme for Diorite Target Plates	35
8	Typical High-speed Photograph of Diorite Ejecta	38
9	Assumed Ejecta Configuration and Velocity Distribution	39
10	Typical Ejecta as Viewed by Quantimet 720 Unit	41
11	Histogram of Particle Fraction versus Size for Run D180 Assumed Spherical Particle Shape	46
12	Probabilistic Ejecta Distribution for Run D180	47
13	Energy Input versus Mean Particle Size for Three Particle Shapes	49
14	Comparison of Measured and Predicted Tangential Strain Histories for Run D180	61
15	Typical Contour Map of a Diorite Crater	62
16	Typical CALCOMP Plot of the Cross-sectional Crack Distribution	64
17	Typical Photographs of Dyed Samples	66
18	High-speed Photograph of a Typical Shale Test	73
19	Section of Shale Sample Struck by a 1/4 inch Diameter Steel Sphere at a Velocity of 5300 ft/sec. Crater filled with a catalyzed methylmethacrylate glue prior to sectioning.	80

<u>Figure</u>	<u>Title</u>	<u>Page</u>
20	Penetration Depth as a Function of Initial Projectile Momentum for Shale	82
21	Square of Penetration Depth as a Function of Initial Projectile Energy for Shale	83

LIST OF TABLES

<u>Table</u>	<u>Title</u>	<u>Page</u>
1	Mechanical Properties of Shale	16
2	Mechanical Properties of Diorite	17
3	Impact Plate Thickness and Strain Gage Locations	21
4	Semi-Conductor Strain Gage Specifications	22
5	Ejecta Cloud Characteristics	37
6a	Ejecta Calculations for Run D180. Disk with height = 0.3 radius	43
6b	Ejecta Calculations for Run D180. Disk with height = 0.5 radius	44
6c	Ejecta Calculations for Run D180. Sphere	45
7	Mean and Standard Deviation of Ejecta Surface Areas for Three Particle Shapes	48
8	Diorite Test Results	50
9	Summary of Wave Energy Calculations	57
10	Crack Surface Areas Based on Various Assumptions	67
11	Comminution Energy per Unit of New Surface Area	70
12	Comminution Constants Based on Quasi-static Theories	71
13	Dynamic Shale Penetration Data for a $\frac{1}{4}$ -in. Diameter Steel Sphere	75
14	Quasi-static Penetration Tests on Shale	78

SECTION I

INTRODUCTION

The state of the art in the field of fragmentation or comminution of rock is not highly developed, yet this process is of extreme importance in a variety of military and civilian applications. Furthermore, the phenomena incident to comminution produced by impact are even less well understood than those associated with quasi-static, more or less steady state events such as occur in mechanical size reduction procedures, yet the former constitute an area of considerable interest to those concerned with the effects of weapons. In particular, the impact of a projectile or the transient loadings caused by an offensive device on the surface of a consolidated geological material produce extremely complicated phenomena. The present document reports an investigation that was designed to provide some information on the mechanical aspects of this problem believed to be of importance in an understanding of the dynamic comminution process.

Comminution as a field of study has a history of more than one century, but has been almost exclusively directed towards industrial applications. Two early theories pertaining to the energy required for the size reduction process were proposed by Rittinger^[1] and Kick^[2]; a third hypothesis was advanced 70 years later by Bond^[3], and a more recent version of a more inclusive nature was presented by Walker^[4]. These expressions are based principally on dimensional analyses and do not pretend to portray an appropriate phenomenological model of the process. The vast reservoir of experimental information derived in the interim has been concerned with energy requirements for crushing and grinding operations and the resultant particle size distributions for a variety of brittle materials^{[5][6][7]}. Virtually none of these studies relate to the problem of rock disintegration under conditions of impact, and it cannot be assumed a priority that such quasi-static results can be applied to projectile impact on geological materials.

Such an event involves a complicated sequence of mechanical phenomena that predominate over thermal effects, in contrast to the case of nuclear explosions where thermal and radiation energies are highly significant.

The impact case consists of a local dynamic contact problem which results in wave propagation in the target that produces motion, strain, cracking, ejection of particles, compaction and crater formation. It may also produce plastic deformation and/or shattering of the striker when certain combinations of high-velocity impact and material hardness prevail; the former did not occur to any measurable degree and the latter situation was found only in one special sequence of the present series of experiments. The investigation described addresses itself to the measurement, data analysis and explanation of these various aspects.

This document constitutes the final technical report for the work performed under contract No. DNA001-73-C-0226 between the University of California, Berkeley, and the Defense Nuclear Agency who supported the activity under NWE D, Subtask Code Y990AXSA001, Work Unit Code 42. It completes the work described in document DNA 3416Z, an interim report for the period 15 May 1973 - 14 May 1974, and covers the interval up to 30 November 1975^[8]. The essential features of the research involved the following topics:

1. The examination of the process of comminution in rocks by experimentally determining the mechanisms relating to the fragmentation process when a striker impinges the plane surface of a block of this material. In part, this was to be accomplished through the use of high-speed photography that would provide a measure of the ejecta velocity and angle of ejection as well as the projectile velocities. The particle size distribution was determined by analysis of the collected ejecta and its spatial distribution was also ascertained.

2. An energy balance of the overall phenomenon was performed in order to attempt to obtain a value of the energy required to produce unit new surface. To execute this calculation, it was necessary to measure the kinetic and strain energy transmitted to the target by wave processes and to assess the magnitude of the new surfaces generated. This involved the employment of a simple model of the ejecta geometry as characterized by a single spatial parameter in conjunction with the measured particle size distribution. It was also possible to identify those aspects of the phenomenon exhibiting very small energy components that could be neglected in the calculations.

3. Within the framework of the overall effort on this problem, the possibility of scaling the event in terms of frequently-employed mechanical variables was examined for wide variations in velocity and geometries of the strikers.

While the objective of the task was initially directed towards the examination of the behavior pattern in soft rocks, considerable effort was also expended on an analogous study of hard rock response to impact. Tests involving the first type of target required the measurement of projectile penetration as well as ejecta, although the latter was found to be very small in a number of experiments implying that the major mechanism of penetration was due to material compaction; some quasi-static penetration studies were also performed. In contrast, the ejecta formed in the hard rocks produced sizable shallow craters whose topography, including volume, were ascertained.

The work on this project involved a collaborative effort with the Naval Weapons Center, China Lake, California that was completely reported in the interim document and will not be repeated here. Close cooperation was also maintained with the Geophysics Group at the Stanford Research Institute, Menlo Park, California, as requested in the contract for the second year. A series of experiments involving novaculite was performed for this group in the laboratories at Berkeley whose results are presented in the final report^[9]. This activity required considerable modification of the equipment and procedure that will be briefly described in the sequel.

SECTION II

SUMMARY OF FIRST YEAR ACTIVITY

The investigation during the first year of the contract was performed both in the laboratories at the University of California, Berkeley, and at the Naval Weapons Center, China Lake, California. While a full and complete account of this activity is described in Reference [8], a summary of this work featuring the highlights and essential results will be presented in the sequel.

The principal experimental apparatus for the comminution studies in

the Berkeley laboratories consisted of a ballistic pendulum with attached target that was struck by a $1/4$ inch diameter steel sphere projectile fired from a pneumatic propulsion device at velocities ranging from about 450 to 700 ft/sec. The velocity of the projectile was measured by the signal produced from the interruption of two light beams, 6 inches apart, traversing two slots in the gun barrel near the muzzle end. Passage of the striker upon exit from the barrel through the beam of a laser also provided a signal which, upon proper delay, activated the discharge of a condenser bank into a flash unit serving as the illumination for the photographic recording of the event by a high-speed Beckman-Whitley framing camera. The targets consisted of shale, limestone or diorite rock samples with a diameter of $5-1/2$ inches and a thickness of $1-1/2$ inches, the first being encased in a matrix of plaster of Paris, while the latter was unconfined; both types of samples had a short aluminum cylinder glued to the center of their top surfaces for attachment to the pendulum. The swing of the latter was measured by a potentiometer and recorded on an oscilloscope.

The ejecta produced by the impact formed a distinctive cloud, a portion of which was trapped on a $10-1/8$ inch diameter lucite plate coated with a polymeric agar to a depth of $1/4$ inch, located approximately 2 inches from the initial pendulum position. Particles not caught on this plate were arrested by a plastic tube with an inside diameter of $11-3/4$ inches and a length of $21-1/4$ inches that completely enveloped the rock sample and plate.

The photographic data, obtained on 79 frames each with dimensions of about 1 cm x 2.5 cm at rates ranging from 50,000 to 190,000 frames per second permitted the determination of the initial and final striker velocity, the contact history of the ball, and the characteristics of the debris generated. The ejecta formed a cloud of fine particles as well as some larger fragments that could be individually identified in a sequence of frames. The speed of the ejecta was calculated in the plane normal to the camera, that for the front of the rock cloud being taken as the average of the values along three rays with due consideration for the shape of this cloud. The softer rocks, shale and limestone, both exhibited a cylindrical ejecta pattern, while that of the diorite formed a conical shell. The velocity of the larger fragments

was also determined on the basis of uniform rectilinear motion, although this is only a crude approximation in view of the known particle deceleration and some observed rotation of the larger fragments.

Results from the film also permitted the calculation of the initial and rebound energy of the striker together with an estimate of the kinetic energy of the ejecta. The particles entrapped on the catcher plate were analyzed with respect to spatial distribution by means of an electronic scanner, which sampled specified plate regions with respect to particle size, area, perimeter, and a shape factor relative to a circular configuration. Particles not so caught, but collected in the plastic tube were weighed and also subjected to analysis by the scanning unit.

An energy balance was executed on the basis of the relation

$$E_{bi} = E_{bf} + E_r + E_{cl} + E_{pend} + E_{com} + E_{fr} + E_{pl} + E_o \quad (1)$$

where the first term is the initial striker energy, and the terms on the right-hand side represent, respectively: the terminal striker energy; that of the larger, separately identified rock fragments; the kinetic energy of the cloud; that of the pendulum; the energy of comminution (i.e., separation energy of the ejecta), the energy of crack formation in the target; that of plastic target and projectile deformation; and other energies, principally that of elastic waves in hard rock targets. In the initial calculations, the energy of plastic deformation and wave energy were neglected. In none of the first year tests was any evidence found to indicate the presence of projectile deformation. However, estimates based on strain measurements on the target surface showed that the wave energy in hard rocks was not negligible. Furthermore, although no plastic deformation of the hard rock samples was noted, a great deal of compaction was found to exist in the shale targets. With the omission of the above energies, it was stated that 99 percent of the initial kinetic energy of the striker was converted into comminution and fracture for the shale, although this figure in reality also includes the very sizeable energy of deformation component. On the other hand, for limestone and diorite where only negligible compaction was observed, the comminution and fracture energy was found to be 94 percent and 80 percent, respectively, based on the same method of calculation.

The significant amount of material compaction in the shale samples was evidenced by the fact that circular lines drawn initially around the impact point were subsequently found at the bottom of the nearly uniform depression. The crater topography was measured by stereotactic means over a discrete net of points using a feeler gage. The data obtained in this manner constituted the input to a computer program that calculates both hole volume and a contour map. The crater volume was also determined by means of fluid or solid filler materials for compact and porous rocks, respectively, and in addition, by an estimate based on micrometric measurements of the maximum and minimum dimensions of the crater near the surface and the maximum depth. The shape of the crater in shale was nearly hemispherical, with a circular surface contour, while that for diorite was conically shaped; the volume for the former material was about one order of magnitude larger than for the harder rock in the case of identical impact situations.

The surface area distribution for fields examined at radii of 5, 50, 100 and 105 mm from the center of the catcher plate could generally be represented by a triangular (or, alternatively, by a Gaussian) distribution on a logarithmic scale for angles of ejection of 0, 45, 90, 135, 180, 225, 270 and 315 degrees. For a range of surface areas from about 20 to 60,000 μ^2 the maximum number of particles involved was 140, 80, 80, 50, 40, 40, 70, and 210, respectively (See Figs. 12a-12h, Reference [8]). Most of the particles were trapped in the region of the largest plate radius rather than in the central region; thus, many shale fragments were not caught by the arresting plate as was also indicated by the substantial amount of debris remaining in the tube.

The zonal surface area of the particles for the shale was found to vary linearly with radius of the catcher plate except when the latter was moved very close to the target; in this case, the peak value of the annular surface area did not occur at, albeit near, the plate edge. However, based on an extrapolation of the data from the ratio of the area scanned by the Quantimet unit to that of the entire catcher plate, about 18 percent of the crater mass of the shale sample was arrested by the plate, with only an additional 10 percent of the mass recovered as fragments in the enveloping plastic tube.

While a large number of dust particles undoubtedly escaped from the system, the major reason for this extreme discrepancy is undoubtedly due to the compaction of the target.

The work performed at China Lake, also detailed in Reference [8], consisted of three separate types of tests, including small-scale laboratory investigations involving 1/4 inch diameter spherical steel projectiles, firings of 20 and 40 mm diameter projectiles from a cannon against the vertical shale cliff of the open pit mine of the American Borax Company at Boron, California, and a single firing of a 6 inch diameter projectile into a reddish silt whose geological properties were believed to closely resemble those of shale.

The small-scale firings were conducted principally into shale disk targets, either plaster-of-Paris encased or enveloped by tape, with diameters of 5.5 inches and thicknesses ranging from 1-1/4 inch to 5.7 inches at velocities up to 8500 ft/sec. Most of the specimens were backed by a metallic disk of identical diameter that prevented rearward spalling. The samples were mounted either on a ballistic pendulum or else on a rigid test stand, the excursion of the former being measured by a precision potentiometer attached to the axis of rotation. The phenomenon was photographed by means of a six-frame Beckman-Whitley Kerr cell type of camera, and the debris liberated by the impact was collected in a polyethylene bag draped over the target configuration.

The impact on the shale produced a cylindrical hole carved out by the projectile almost exclusively as the result of material compaction as well as a cone-shaped or dish-like depression near the surface apparently formed by ejection of particles. By superposing a metal plate with a central hole to permit passage of the projectile on the sample, the surface dishing was virtually eliminated. The ejecta collected under these circumstances amounted to 20-25 percent of the total hole volume, independent of initial velocity; the remainder of the volume had to be attributed to compaction. On the other hand, only dishing occurred in the harder and more brittle rocks such as diorite and spessartite, with some propagation of cracks produced by the impact; compaction, plastic deformation or distortion of both target and striker are so small as to be negligible.

Sectioning of the damaged targets was performed after filling the hole with a clear epoxy mixture to avoid further breakage. This filler also clearly delineated the region of compaction, which consisted of a bell-shaped zone around the hole with its tip approximately one radius ahead of the terminal projectile position.

A total of 46 rounds was fired in this sequence of experiments, including preliminary tests involving diorite and spessartite targets. The crater depth was found to vary linearly and the crater volume as the square of the initial velocity, with large deviations occurring only upon shattering of the projectile; the latter event occurred only at extreme velocities. The volume of the surface dish was found to vary between 30 and 80 percent of the total crater volume without any apparent relation to initial velocity; in all cases, an extensive network of cracks was produced that frequently extended to the lateral specimen surfaces.

The fragment velocity was found to increase with rising initial projectile speed, and the angle of ejection was noted to decrease correspondingly from a magnitude of about 60° in the range from 2000 to 3000 ft/sec to an angle of 35° at the maximum velocity of about 8200 ft/sec. In addition to the symmetric particle cloud forming an outer conical shell that was subsequently transformed into a double envelope, a central initially circular region of particles was photographed that was believed to be the result of high turbulence inducing vortex formation. The sieving of the debris by a series of meshes did not result in a Gaussian distribution.

A total of 18 rounds was fired from tank guns using 20 mm rifled and 40 mm rifled and unrifled projectiles with standard ogival noses against fresh vertical shale surfaces of the Boron open pit mine at initial velocities ranging from 2000 to 2900 ft/sec as determined by the piercing of electrically wired screens. This provided an initial kinetic energy ranging from 0.30- 2.33×10^5 ft-lbs compared to a value of 0.000012×10^5 ft-lbs for the 1/4 inch diameter steel spheres fired at 185 ft/sec. The phenomenon was photographed by two Fastax cameras operating at nominal framing rates of 3000 per second, indicating a conical cloud angle of about 60° and maximal fragment velocities of about 700 ft/sec. After clearing the base of the cliff, the

debris ejected by the firing of the round was collected in large plastic sheets and weighed; however, a portion of this material from remote regions of the wall was believed to have been knocked loose by either the sound or shock waves. While, for the 40 mm projectiles at full loads, considerable scatter was found in the penetration depth and the type of trajectory (a number of projectiles veered from their path or began to tumble), consistent results were obtained for 40 mm projectiles with reduced charges and for the 20 mm projectile. Surface dish volume data for all shots were also inconsistent; this might be expected in view of the variable and uncontrollable surface conditions of the various parts of the cliff where shots were attempted. Significant plastic deformation of the cliff was found for all rounds at the entry into the bore hole without, however, leading to changes in density of the substance.

A fair correlation exists between the initial kinetic energy of these larger shots and the weight of shale from the crater; here, most of the material so removed came from the dish, while a larger proportion was displaced from the hole in the small-caliber tests. This is partly due to lateral confinement of the model and the absence of loose or projected sections in the machined samples.

Sieving of the recovered debris also did not yield a Gaussian size or weight distribution; undoubtedly, secondary fragmentation of the material occurred to some extent upon contact with the ground. Only a small fraction of the weight of the material removed from the crater based on calculations involving the hole volume and the initial density was recovered; the remainder was ejected over an area much wider than the ground cloth, and, most importantly, sizeable compression and plastic deformation of the cliff ensued.

A single firing of a 6 inch diameter ogival-nosed steel shell weighing 95.6 lb. into a cohesive reddish silt having a density of 1.52 g/cm^3 was executed at a velocity of 1340 ft/sec. The trajectory was not linear, with a total travel of about 11 feet. The dished region formed a cone with a surface diameter of 3 feet and a depth of 6 inches; the initial diameter of the penetrating hole was identical to that of the projectile. The total crater volume is thus 5615 in^3 with a weight of 308 lb for an initial kinetic energy of $2.68 \times 10^6 \text{ ft-lb}$.

SECTION III

LIAISON WITH STANFORD RESEARCH INSTITUTE

As requested in the contract, close liaison was maintained throughout the year with the Geophysics Group of Stanford Research Institute, particularly Drs. D. Curran and D. Shockey. At their request, a series of tests were performed on the hard rock novaculite using the pneumatic gun and high-speed camera of the Berkeley laboratory. While the samples were furnished by the Stanford group, the experiments required considerable modification of the test arrangement, particularly with respect to the ejecta recovery unit. Additional changes were required to accomodate a device placed on the muzzle end of the gun that insured normal impact of the projectile with the specimen and simultaneously determined the exit velocity. The tool steel projectiles for these experiments shattered upon impact due to the high velocity and their brittle nature. Two of these tests were performed and the data was transmitted to the requesters. The results have been described in the final report of the group, Reference [9].

SECTION IV

WORK PERFORMED DURING THE SECOND CONTRACT YEAR

The principal activity during the second year of operation of the contract was the determination of the energy required to generate unit new surface in the case of impact on hard rocks, the evaluation of the penetration of projectiles in the case of soft rocks, and an attempt to compare the data obtained during the entire course of the investigation with both analytical expressions developed for fragmentation (primarily intended to describe grinding processes) and with parameters scaling the impact intensity. This involved several relatively independent physical aspects of the problem:

(a) The determination of the energy contained in the elastic wave propagating through the specimen, (b) The evaluation of the surface area associated with the ejecta, continuing the endeavors of the first year of operation, (c) The estimation of the new surface generated by the cracks produced in the specimen due to the impact, (d) The crater morphology, and for the soft rock, the

3
penetration depth. Examination of the projectiles subsequent to contact indicated no permanent deformation for any of these tests. In the sequel, the details of this effort will be described.

IV.A. SAMPLE PREPARATION

The rock specimens employed consisted of samples of green shale and diorite, 5-1/2 inch in diameter, both cored by my means of a standard rock drill. The shale was obtained from the site of the open pit mine of the U.S. Borax and Chemical Corporation, Boron, California; the geology and details of sample preparation are give in Reference [8]. The samples were enclosed in plaster of Paris molds with a 6.5 inch square cross section; the specimens were cut with a water-cooled diamond saw to a thickness of 1 inch. The perimeter of the samples was wrapped with friction tape to prevent lateral cracking of the specimens and mold during testing. Table 1 lists pertinent mechanical properties that have been derived for this material.

The diorite acquisition site, mineralogy and sample preparation were also described in Reference [8]; the same procedure, but without encasement, was employed to obtain 1 inch thick samples with the coring and cutting at feeding rates of a few inches per hour. Table 2 presents the mechanical properties of this material; additional information on the mineralogy and properties of this substance are contained in References [10] and [11].

The determination of the energy contained in elastic waves transmitted to the sample required the construction of a reusable specimen with strain gages embedded in the interior. This could not be accomplished for the shale due to its fragility. As shown in Figure 1, this composite consisted of a very thin frontal plate of diorite and a somewhat thicker back-up plate of this material, both of the same diameter, 5.5 inch, as the gaged 1 inch thick specimen. The latter was cut on a diametral plane with a 0.08 inch thick water-cooled diamond saw, lapped to 4/0 grain size using standard procedures, and three radial strain gages were then cemented along the axis of symmetry as indicated. No. 38 enamel-coated leads with a diameter of 0.004 inch and a resistance of 0.660 ohm/foot were attached to the gage wires and brought out along a diameter of the section. The two halves of the specimen were then glued together with 3M structural epoxy, forming a joint

TABLE 1. MATERIAL PROPERTIES OF SHALE

Property	
Mass Density, ρ	2.25 g/cc
Poisson's ratio, ν	0.25
Young's Modulus, E	$1-3.5 \times 10^9 \text{ N/m}^2$
Dilatational Wave Velocity, c_D	1500 m/sec
Compressive Strength	$10^6 - 10^7 \text{ N/m}^2$
Lamé Constant, λ	$0.4 - 1.4 \times 10^9 \text{ N/m}^2$
Lamé Constant, G	$0.4 - 1.4 \times 10^9 \text{ N/m}^2$
Porosity	10-30%

TABLE 2. MATERIAL PROPERTIES OF DIORITE

Property	
Mass Density, ρ	2.67 gm/cc
Poisson's ratio, ν	0.25
Young's Modulus, E	3.80×10^{10} N/m ²
Dilatational Wave Velocity, c_D	4140 m/sec
Compressive Strength	2.21×10^8 N/m ²
Average Grain Size	1.5 - 2.0 mm
Lamé Constant, λ	1.52×10^{10} N/m ²
Lamé Constant, G	1.52×10^{10} N/m ²

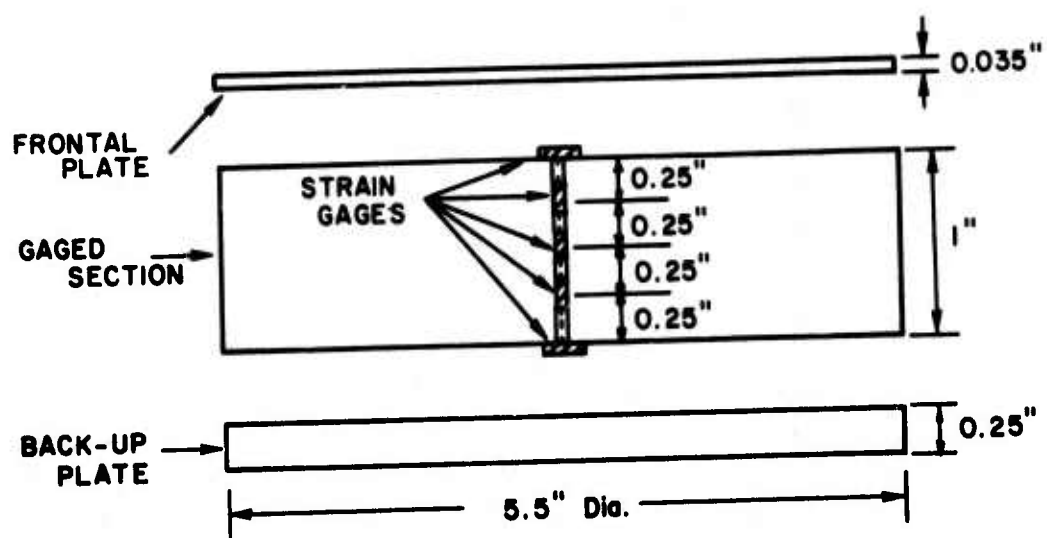


Fig. 1 - Composite Test Specimen with Embedded Gages

0.1 inch thick that was cured for at least one day and whose rough edges were smoothed with increasing grades of fineness of emery cloth. One tangential gage was then glued to each of the top and bottom surfaces at the center, as shown in Figure 1, and lead wires were again attached and brought to the outside of the composite in a similar manner.

Several other 1 inch x 5.5 inch diameter diorite disks were further cut to various thicknesses with a 1/8 inch thick oil-cooled diamond saw at a rate of a few inches per hour. Two of these were the 0.035 inch thick target face plate and the 1/4 inch thick back-up plate which were permanently bonded to the front and back of the gaged section, respectively, after both sides had been lapped as described above. A nominal 3/4 inch thick diorite transmission plate was then wrung on with grease to the rear of the back-up plate, and a number of impact plates ranging in thickness from 0.205 inch to 0.434 inch, that essentially constituted the sample undergoing comminution, was also wrung on with grease to the front of the target face plate. Finally, this diorite composite was wrung with grease onto an 11 inch diameter aluminum back-up plate consisting of 2 disks with a total thickness of 4.5 inches to serve as a wave trap. To insure intimate contact of the greased faces, the unit sat under its own weight for some time prior to testing, so as to permit the escape of air bubbles and excess grease from the joints. The complete assembly is shown in Figure 2; Table 3 gives a description of the specimen properties and the distance of the five strain gages from the impact point which was located at the center of the front surface of the impact plate.

The five strain gages, denoted as 1R, 2R and 3R for the radial transducers and 1T and 2T for the tangential ones, consisted of SPB-3-12-12 semiconductor gages manufactured by Baldwin-Lima-Hamilton with a nominal gage length of 1/8 inch, an unstrained resistance of 128.2 ohms \pm 1 percent and a gage factor of 117.3, according to the manufacturer. The gages were cemented with Baldwin-Lima-Hamilton gage epoxy. Table 4 presents the measured circuit resistance for each transducer at two times during the period of investigation. Each gage was incorporated in a potentiometric circuit activated by a 24-volt battery with a 2120 ohm ballast resistor that reduced the voltage across each gage and thus prevented their overheating. Each gage was calibrated after

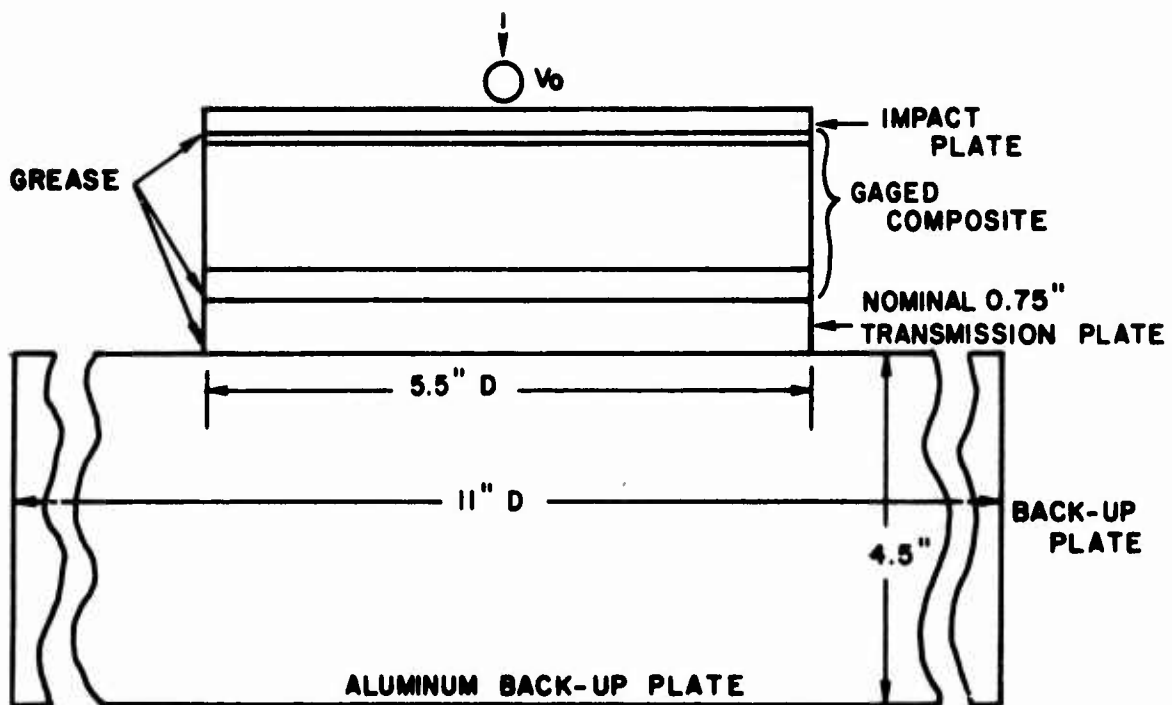


Fig. 2. - Assembly of Composite Duroite Sample

TABLE 3. IMPACT PLATE THICKNESS AND GAGE LOCATIONS

Sample	Average Thickness, in.	Maximum Deviation, in.	Distance from Impact Point to Gage, in.			
			Gage	IT	IR	2R 3R 2T
D 100	0.274	± 0.003		0.309	0.559	0.809 1.059 1.309
D 120	0.351	± 0.050		0.386	0.636	0.886 1.136 1.386
D 140	0.350	± 0.048		0.385	0.635	0.885 1.135 1.385
D 160	0.273	± 0.003		0.308	0.558	0.808 1.058 1.308
D 180	0.408	± 0.011		0.443	0.693	0.943 1.193 1.443
D 200	0.363	± 0.013		0.398	0.648	0.898 1.148 1.398
D 220	0.368	± 0.040		0.403	0.653	0.903 1.153 1.403
D 240	0.434	± 0.012		0.469	0.719	0.969 1.219 1.469

TABLE 4. SEMI-CONDUCTOR STRAIN GAGE SPECIFICATIONS

Strain Gage	Gage Coordinate, r, in.	(1) Orientation	Manufacturer's Gage Data			Gage Factor Used, GF	(2) Resistance, R _B , ohms
			Type	R _O , ohms	C ₂ ¹	GF ¹	
1T	0.135	ε _{θθ}	SPB3-12-12	128.2	4600	117.0	119.9
1R	0.285	ε _{rr}	SPB3-12-12	127.4	4500	117.3	123.3
2R	0.535	ε _{rr}	SPB3-12-12	127.4	4500	117.3	122.5
3R	0.785	ε _{rr}	SPB3-12-12	127.4	4500	117.3	122.2
2T	1.035	ε _{θθ}	SPB3-12-12	127.4	4500	117.3	120.6
							114.3

(1) Displacement on centerline from front of gaged composite.

(2) Type of strain to be measured.

(3) Gage Factor used is: $GF = \frac{R_O}{R_B} \left[GF^1 + C_2^1 (2\epsilon_B + \epsilon_{max}) \right]$ where ϵ_B is determined from tables

supplied with the strain gages.

every test by the rapid shunting of a sequence of known parallel resistors with the response recorded on an oscilloscope providing the scale factor for the strain^[12].

IV.B. EXPERIMENTAL APPARATUS AND PROCEDURE

The experimental apparatus employed for the present comminution studies of rock by mechanical impact consists essentially of a pneumatic gun resting on a heavy steel table, a wooden stand on which the sample and aluminum back-up cylinder are placed, a high-speed camera with a framing rate continuously adjustable from 20,000 to 1 million per second, associated triggering devices, strain measuring transducers and associated recording equipment. A schematic of the arrangement is presented in Figure 3, and Figure 4 shows a photograph of the set-up. The compressed gas gun features a 1/4 inch inside diameter steel barrel with a length of approximately 54 inches and utilizes either compressed house air with an upper limit of 180 psi or nitrogen as the driving mechanism. The latter gas is withdrawn from a standard bottle, initially compressed to a pressure of 2250 psi, through a control panel to a reservoir behind the breech that is isolated from the barrel by an electromagnetic valve with an upper limit of 1500 psi capacity. An electrical noise suppressor was employed in series with the valve switch to prevent the appearance of large electrical transients due to valve activation on the oscillographic records. The muzzle velocity of the 1/4 inch diameter steel spheres employed as strikers in the present experiments is controlled by the chamber pressure that is adjusted by a regulator on the panel. Firing of the projectile inserted in the gun muzzle occurs by opening the electromagnetic valve, permitting discharge of the gas in the reservoir and acceleration of the projectile; subsequently, the valve is closed automatically to prevent waste of the bottled nitrogen.

Two horizontal slots cut into the walls of the barrel near the muzzle end permit the passage of two light beams at a fixed distance 6 inches apart that are focused on two photo-diodes whose output is connected to a type 3A1 dual trace amplifier and monitored on a Tektronix type 565 oscilloscope. Interruption of the beams by the passage of the projectile generate flat-topped transients with a rise time of about 10-20 microseconds that can be

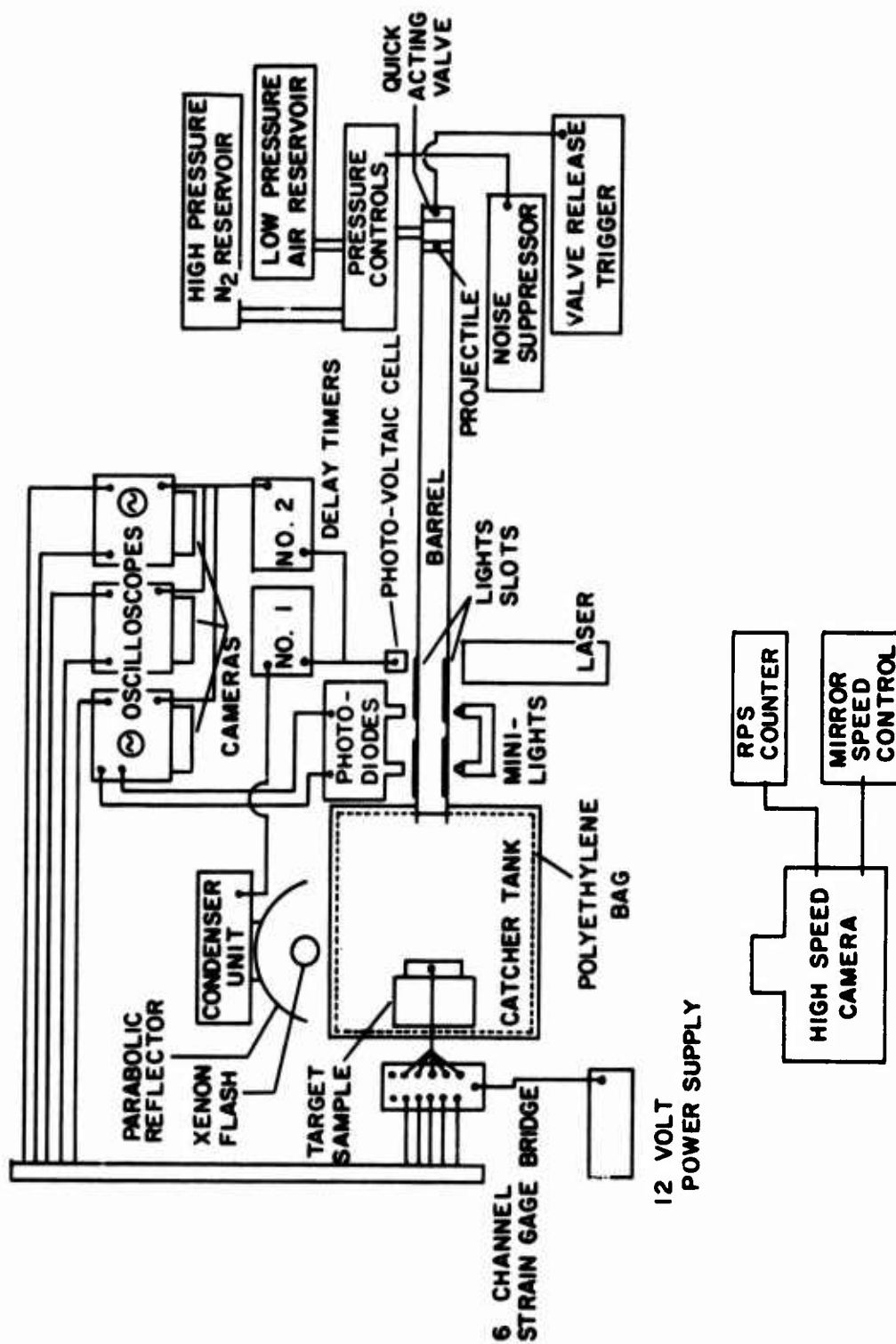


Fig. 3 - Schematic of the Experimental Arrangement

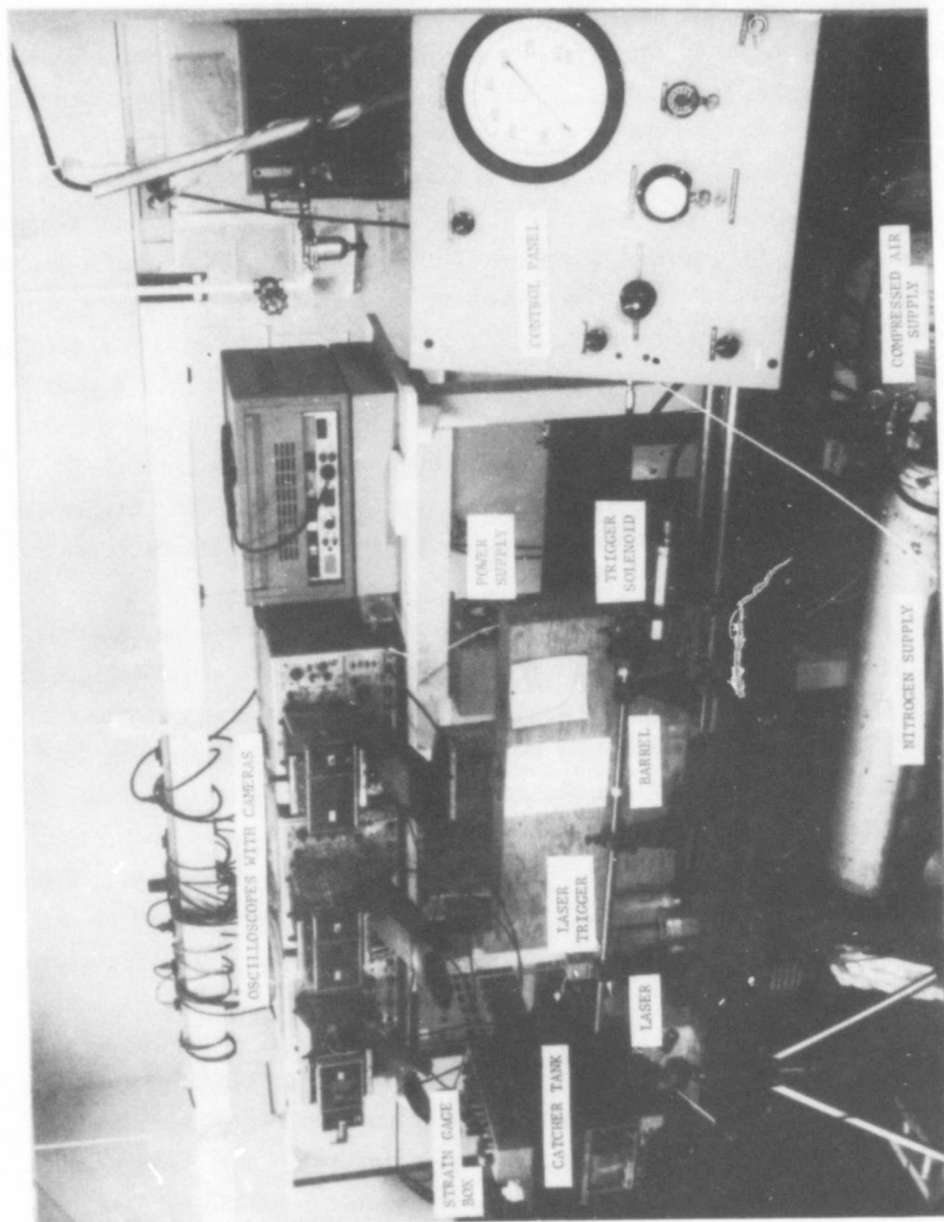


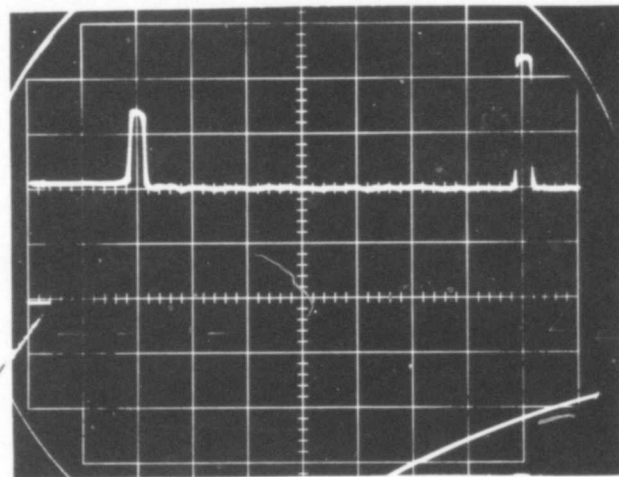
Fig. 4 - Photograph of the
Experimental Arrangement

employed to reliably measure the projectile velocity. A typical photograph of the oscilloscope record of this device is shown in Figure 5. A helium-neon laser beam was directed through the slot nearest the breech onto a photovoltaic cell that produces a signal sufficient to trigger delay time units incorporated in the Tektronix 565 dual-beam oscilloscopes.

The first delay timer provides for the discharge of a 70 μ f, 4.8 kV condenser bank into a General Electric FT 524 flash tube activated through a thyatron tube^[12]. This event simultaneously serves as a shutter and a light source for the operation of the Beckman-Whitley WB-2 camera which has 79 independent frames. The speed of the rotating prism in the camera is controlled by a rheostat and is displayed on an electronic revolution counter. A parabolic reflector collects the light and passes it through a sand-blasted plate of plexiglass which acts as a diffuser and produces a nearly uniform field of illumination on the target. The second delay timer acts as the trigger for the remaining five oscilloscope channels so as to capture the start of the strain gage signal.

The delay setting was critical due to the extremely short time interval, 200 μ s, during which the initial portion of the strain signal could be viewed with an acceptable resolution relative to the delay time interval of about 1500 μ s for the camera and 1600 μ s for the gages. In order to properly determine the magnitude of this delay, a device was developed consisting of two pieces of aluminum foil 2 inches square which were placed, one on each side, over a 1 inch square hole cut in a piece of 1/16 inch thick plexiglass. When this foil was struck by the projectile in a preliminary test designed to set the proper delay, the two pieces of foil touched and completed the circuit to produce a voltage spike from a suitable generator.

The agar plate and surrounding plastic tube arrangement previously employed to capture the ejecta from the target plate was replaced by a system consisting of a thin polyethylene liner placed around the target and the gun in such manner as to completely encase the region initially traversed by the ejecta. This liner was positioned inside a rectangular metallic catcher tank covered on the interior with foam sheets that served as a cushion to reduce additional fragmentation of ejecta upon contact. The polyethylene sheets were



Velocity Measurement

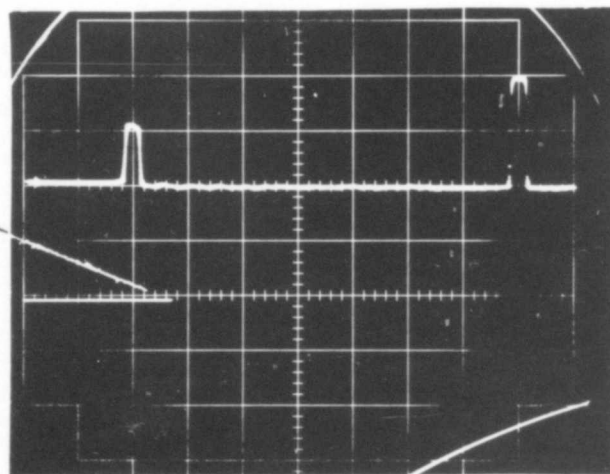
Sweep: 100 μ sec/div

Delay Measurement

Sweep: 20 μ sec/div

Delay Time: 1760 μ sec

Trigger Signal



Velocity Measurement

Sweep: 100 μ sec/div

Delay Measurement

Sweep: 20 μ sec/div

Delay Time: 1780 μ sec

Fig. 5 - Typical Photographic Records of
the Initial Velocity and Delay Measurements
for Run D180

stretched over a thin metallic frame contained within the tank. This arrangement was not totally effective in capturing the entire mass ejected from the target, since some of the particles perforated the container lining and embedded themselves in the foam from which they could not be readily recovered. The tank was supplied with two viewing ports that permitted photography of the comminution event.

The collision of the striker with the target produced comminution of the rock in various degrees, accompanied by crater formation, penetration or both, depending on the nature of the target material. When the projectile is not embedded, as occurred invariably in the lower velocity tests conducted more recently, the striker rebounds with diminished velocity after a contact period of the order of microseconds, simultaneously with any ejecta produced. Concurrently, energy is transferred to the interior of the sample in the form of strain waves that could produce damage in regions remote from the contact point.

The experimental procedure diverged somewhat depending upon whether diorite or shale targets were employed. In the former case, the composite system including the aluminum backup plate was placed on a contoured wooden stand inside the catcher tank with the impact face positioned within the viewing area permitted by the ports. The shale targets, which consisted of single potted and taped disks, were supported in a similar fashion except that they were not greased to the back-up plate, but clamped to it. In view of the lack of significant ejecta formation for this target, the trajectory of the debris from this type of specimen was not determined from photographs during the second year of operation. Typical high speed photographs were presented in Reference [8].

Thus, the tests on the diorite targets involved the simultaneous determination of the initial striker speed from time interval data, the final projectile velocity and debris kinematics by means of high-speed photography, crater topography measurement by means of feeler gages, ejecta size distribution by electronic scanning methods, elastic wave energy in the target from internal strain histories and crack production in the sample by post mortem sectioning. On the other hand, for the shale, only impact velocity of the projectile and penetration depths were determined.

For the photographic measurements, the high speed camera was located 66-1/2 inches from the impact area and recorded the data on a 5 foot length of 35 mm Tri-X film which was transferred into the stationary film holder from the storage cassette. The data obtained in this fashion includes the history of the striker before impact, the contact of the ball with the rock, the displacement history of the rebounding projectile, and the trajectory of the debris generated for a period of about 600 μ s, thus involving a framing rate of 132,000 per second. The ejecta consists of a cloud of fine particles, appearing in the form of a conical shell, as well as of some larger fragments. The area appearing in the photographs, between the sample and the end of the gun barrel, lies in the vertical plane normal to the target and is about 4-1/4 inches high by 2-1/8 inches wide.

The frontal position of the cloud was traced along the extreme rays and the velocity of the fastest particle was ascertained. With certain assumptions, this permits the evaluation of the kinetic energy of the fragments and the rebound energy of the ball. The former was facilitated with the aid of a computer program^[8] that requires as its input the position-time information contained in the photographs. Development of the film occurred in a Microdol X solution diluted in the ratio of 1:3 to provide minimum graininess in enlargements of the photographs. Such blow-ups were produced on polycontrast paper with a magnification of 6.5 to 7, and all required information was determined from these enlargements.

Concentric circles of 1/8, 1/4, 3/8, 1/2, 3/4 and 1 inch diameter were drawn with india ink about the contact point of the diorite and with pencil on many of the shale targets. For diorite, the volume and the net surface area of the craters were determined by depth measurements using feeler gages over a 10 x 10 mesh, that were recorded on a Tektronix D13 dual beam oscilloscope with AM 502 and 5A22N differential amplifiers. These data served as the input for a computer program^[8] that calculated these variables and also plotted a contour map which provides a reasonable three-dimensional representation of the crater.

In the plurality of the low-velocity tests using a 1/4 inch diameter steel sphere as a projectile, the crater produced in the shale samples

consisted of a hemispherical indentation with short (i.e., less than striker radius) cylindrical stems emanating to the surface. In some cases, a shallow dish was additionally formed at the intersection of the stem and the target face. A few tests employing larger projectile diameters resulted in severe cracking of the entire sample and surrounding material and were thus discontinued. In view of the minor role of the dish and the brittleness of the material, only maximum penetration measurements were executed by means of feeler gages in the shale targets.

The diorite ejecta trapped in the catcher tank was carefully transferred to a petri dish and weighed. With the assumptions that the density of the ejecta is identical to that of the material in the original regions of the crater and that no compaction takes place in the target, a mass scale factor was computed that related the material recaptured to the total ejected; as explained previously, some particles escaped entrapment and others might have been lost during the transfer process. Since the shale exhibited significant permanent deformation, it was not possible to utilize this procedure for this material. The shale ejecta was also collected and weighed, but its size distribution was not analyzed.

The collected diorite particles were distributed randomly on a 5961 mm^2 glass plate that was then subjected to mild agitation. The plate had been coated with an anti-static spray so that conglomeration of the particles and concentrations near the perimeter of the viewing area would be avoided. A region amounting to 34.6 percent of the plate area was surveyed by an electronic scanner, a Quantimet 720 unit located on the Davis campus of the University of California. This device is capable of examining specified rectangular fields containing aggregates of particles of diverse shapes and sizes; in the present instance, five $17.9 \text{ mm} \times 22.96 \text{ mm}$ domains were analyzed within the plate region for each of which the number of particles contained in ten distinct intervals of their projected area were enumerated. In contrast, in the first year of operation, several hundred areas, each of 8.15 mm^2 size were sampled by the Quantimet. This information was scaled up both by the area factor consisting of the ratio of total plate area to that electronically scanned, and by the mass factor previously defined.

Simple particle geometries capable of being described by a single dimension, selected from microscopic examination of the ejecta, were utilized to compute surface areas and volumes of the fragmented crater mass based upon the electronically measured distributions.

In general, the sweep rate for the strain gages was chosen as 20 $\mu\text{s}/\text{cm}$ (or, in one case 10 $\mu\text{s}/\text{cm}$), a compromise between adequate resolution, sufficient length of the trace and triggering considerations. The amplification varied from 20 to 100 mv/cm so as to permit the recording of two traces on a single photograph without interference and, further, to avoid a ratio of pulse height to width larger than 2:1. Typical data from these transducers are presented in Figure 6. These traces can be employed to compute the wave energy on the hypothesis that the pulse is hemispherical and propagates in a homogeneous, elastic isotropic medium without reflection from free surfaces.

The present report also addresses itself to an examination of the internal damage below the surface of the crater, a topic not considered in the previous report. While the activity of the last year has shown that the crack network on a typical diametral section can be displayed for measurement purposes, it proved virtually impossible to separate the cracks produced as the result of the impact from those existing previously. Nevertheless, such an examination was executed to establish bounds on the new surface produced as the result of the collision that consists both of ejecta and crack formation.

Thus, the 5.5 inch diameter target plates were sectioned through the maximum crater diameter using a 0.08 inch thick water-cooled diamond saw; this section was further cut to a width of 2.5 inches to permit machining. The region on this section below the crater was then lapped using progressively finer grades of emery paper from #320 to 4/0 grit. The samples were then placed under illumination by a carbon arc on a Unitron metallurgical microscope with a magnification of 13.7. Polaroid film 55 P/N was used to record overlapping sections of the specimens and a composite photograph of the damaged area was produced. All visible cracks occurring in the entire central diametral region were approximated as straight lines whose actual terminal coordinates were digitized by means of a plotting device controlled through a program placed on a PDP-7 computer. The output was processed by means of a

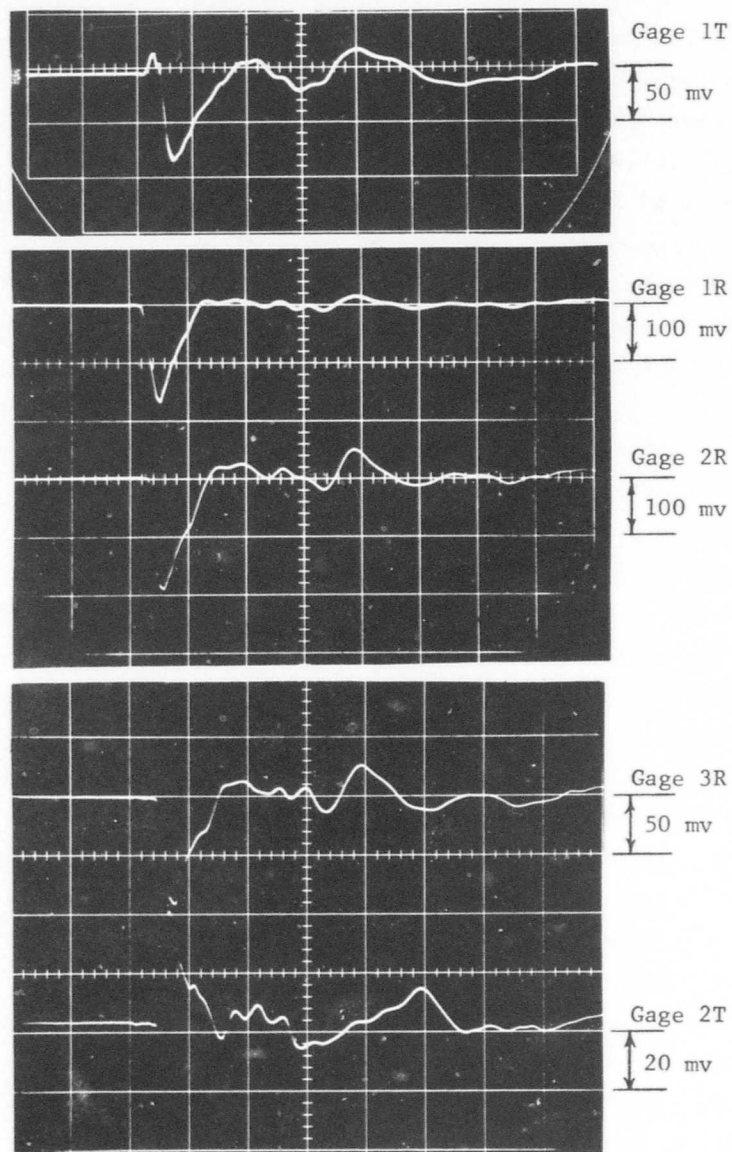


Fig. 6 - Strain Gage Histories as
Measured for Run D180; Sweep Rate:
20 μ sec/div for all gages

program which calculated the cracked surface area based on the hypothesis of an axially-symmetric distribution of cracks; a plotting device, Calcomp, associated with the CDC 6400 computer located on the Berkeley Campus of the University of California, provided an automatic graphical representation of this crack network.

The polished crack samples, an example of which appears in Fig. 7a, were then dyed using Spotcheck dye penetrant manufactured by Magnaflux Corporation, Chicago after cleaning of the section with a solvent; the penetrant was applied as a spray and removed with a cloth after 30 minutes in the case of the fine cracks present. The developer was then sprayed on the surface and allowed to act for a period ranging from 5 to 15 minutes before inspection of the surface; the cracks and pores are brought out as a series of red lines and dots. This pattern was photographed with 55 P/N Polaroid film and enlarged to the same magnification as the composite picture of the damaged area in the undyed specimen, permitting an assessment of the regions and amount of damage. In a similar manner, an area of the section remote from the crater (at least one crater diameter away) was surveyed on the hypothesis that this region was representative of the virgin state of the rock. The difference between these networks was attributed to the impact process.

Several quasi-static tests were conducted on the shale with an Instron machine using various rates of feed. A 4 inch long, 1/4 inch diameter section of drill rod with a hemispherical tip to simulate the shape of the striking sphere was pressed into the sample to obtain a force-indentation relation and to determine if strain-rate effects existed in the quasi-static range. The indentation rate was maintained constant and the force history was recorded by means of a load cell. These data permit the calculation of the energy of penetration as a function of depth.

IV.C. RESULTS AND DISCUSSION

1. Diorite

a. Velocity Measurements

For the most part, the initial velocity of the projectile as determined by the photodiode measurement was higher than that calculated from the high speed camera data; however for two different pressures, the camera data yielded the same velocity.

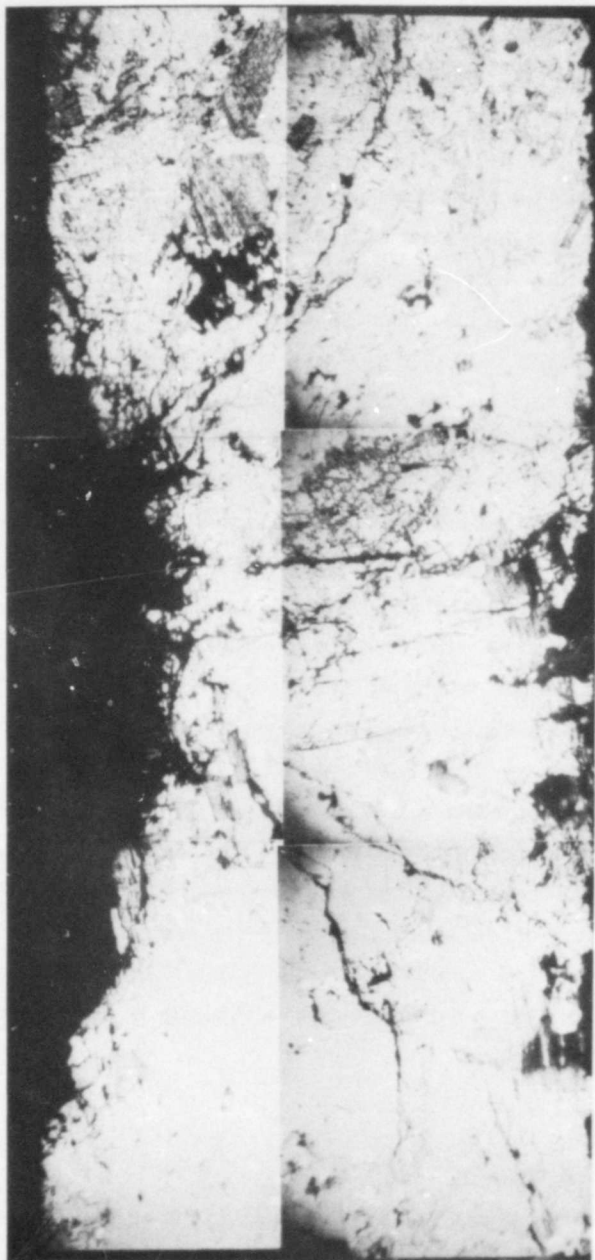


Fig. 7a - Montage of Typical Cross-section of Diorite
Sample After Impact

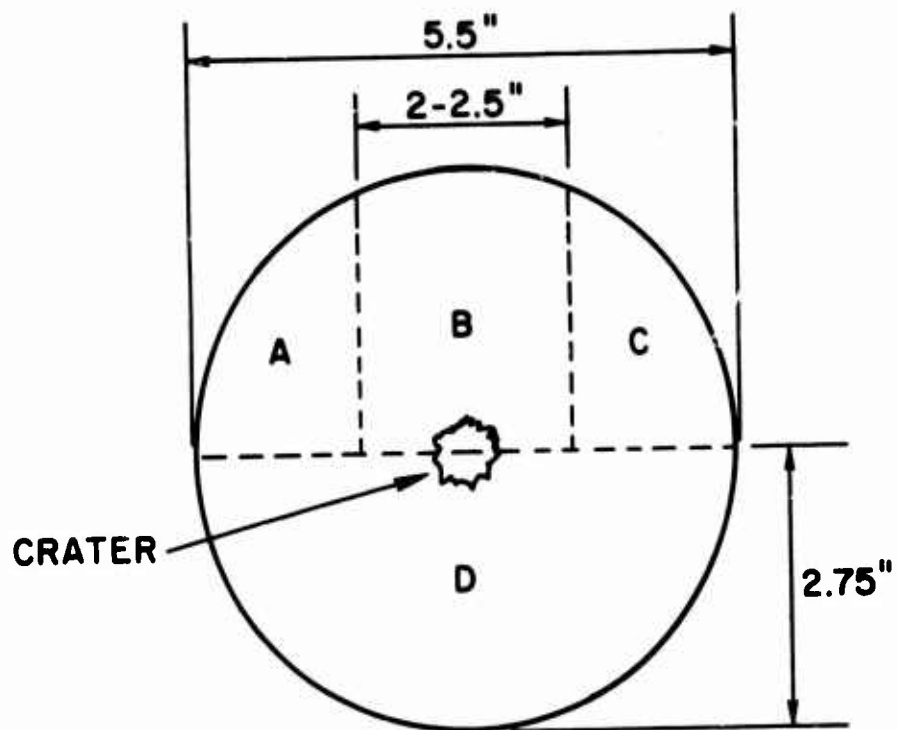


Fig. 7b - Post - Mortem Sectioning Scheme
for the Diorite Target Plates

Since some of the runs yielded an insufficient number of frames for reliable initial velocity measurement from the photographs, the original projectile speed was uniformly obtained from the light beam interruption technique. The camera data was considered to be reliable for the determination of the ejecta and projectile rebound velocities. The velocity of the leading edge of the cloud formed by the ejecta mass is given in Table 5.

b. Ejecta

A typical high-speed photograph of the ejecta cloud is shown in Figure 8. The kinetic energy of these particles was calculated on the assumptions that elemental rings of constant mass, dm , are emitted during impact in the form of a right circular conical shell whose axis is taken along the x -direction, and that the velocity of each ring, v , varies linearly from a maximum measured value v_m at the cloud front to zero at the impact face, as shown in Figure 9 which represents the instant of final ejecta formation when the altitude of the shell is L . These assumptions are considered to be reasonable in view of previous analyses of the spatial particle distribution^[8] and inspection of the present photographs that indicate the cone-like shape of the cloud, and that, further, successively emitted particles move at a consecutively slower rate. In fact, some ejecta were found to be resting in the crater upon inspection after impact.

The energy associated with the element of mass dm is given by

$$dE_{ej} = (1/2)v^2 dm \quad (2)$$

The symmetry of the cloud and the velocity distribution assumption leads to the relations

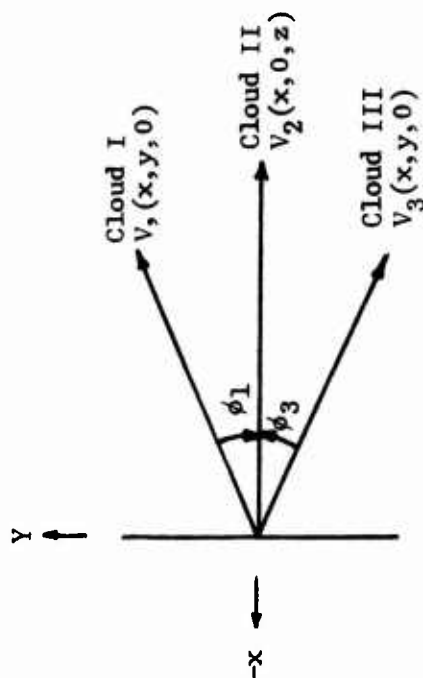
$$v = v_m(x/L) \quad \text{and} \quad dm = (M/L)dx \quad (3)$$

where M is the total ejecta mass, determined on the basis of the measured crater volume. Upon substitution and integration of Equation 2, the total kinetic energy of the ejecta, E_{ej} becomes

$$E_{ej} = (1/6) M v_m^2 \quad (4)$$

TABLE 5. EJECTA CLOUD CHARACTERISTICS

Sample	Cloud I		Cloud III		Cloud II	
	Angle of ejection, deg	Maximum velocity, m/s	Angle of ejection, deg	Maximum velocity, m/s	Angle of ejection, deg	Maximum velocity, m/s
D 100	49.5	141	-51.9	142	± 50.7	140
D 120	56.9	298	-37.4	185	± 47.2	134
D 140	40.4	260	-41.4	241	± 40.9	305
D160	59.8	358	-25.0	183	± 42.4	148
D180	47.5	219	-46.9	267	± 47.2	311
D200	53.3	346	-44.8	266	± 49.1	243
D220	48.0	251	-40.2	262	± 44.1	252
D240	60.1	159	-37.9	214	± 49.0	200



ϕ_1 and ϕ_3 measured from high speed photographs; ϕ_2 determined from $\phi_2 = \frac{\phi_1 + \phi_3}{2}$

$$\text{with } V_2 = \frac{V_2(x, 0, z)}{\cos \phi_2}$$

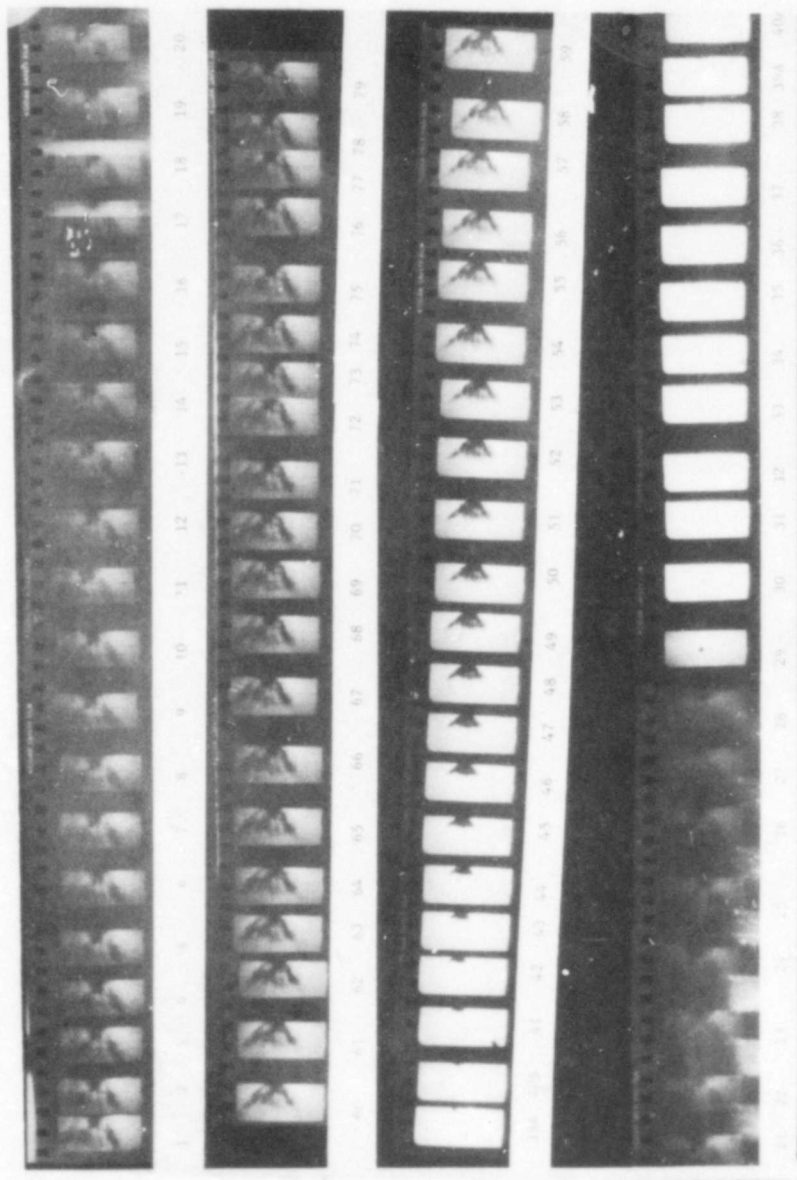


Fig. 8 - Typical History of Ejecta
Formation for Diorite, Run D180

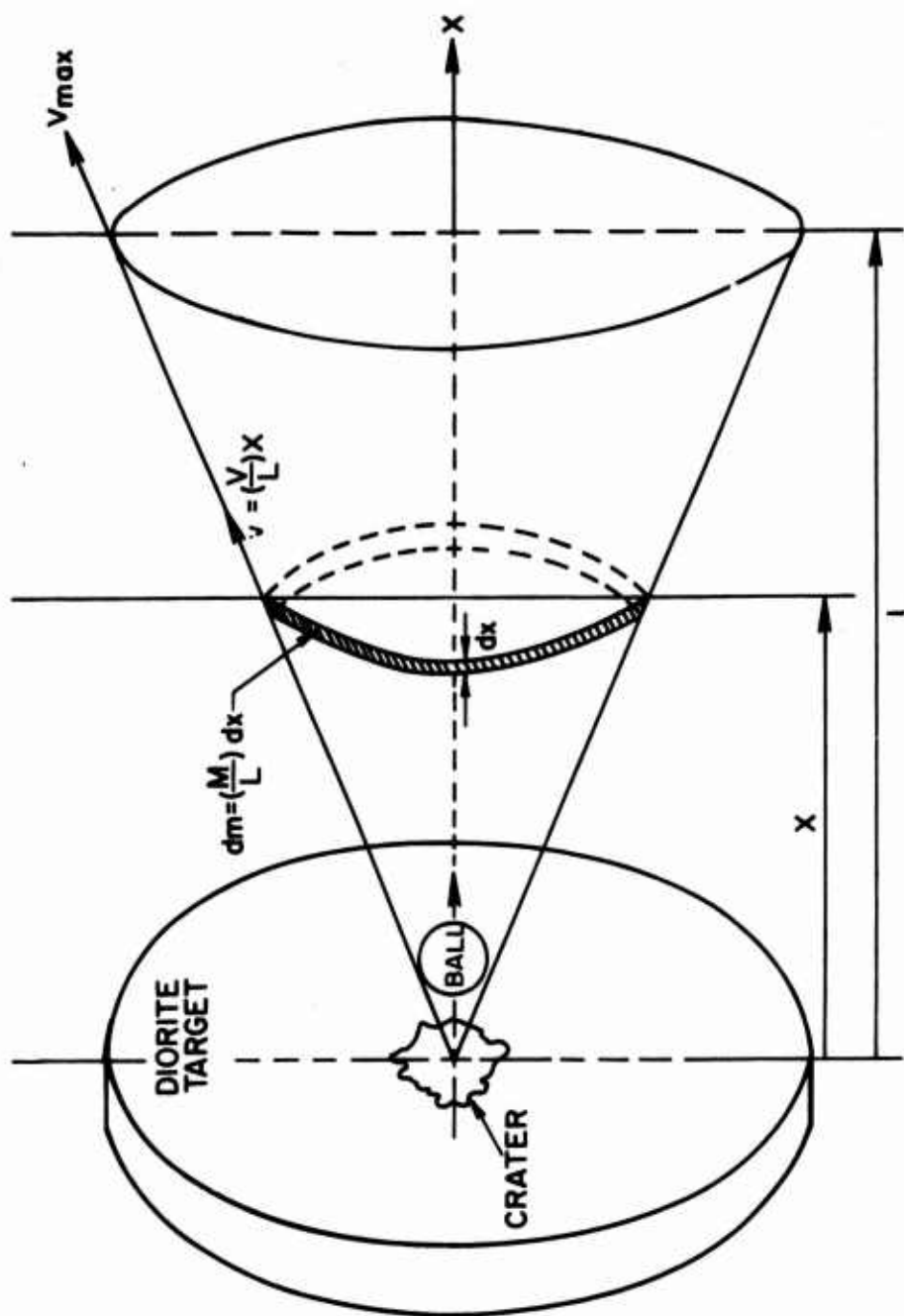


Fig. 9 - Assumed Ejecta Configuration and Velocity Distribution

While this appears to be a reasonable estimate, it is considered to be a lower bound value in view of the prescribed velocity distribution. However, this hypothesis is much more reasonable than the use of a constant value of the velocity v_m for each particle of the cloud, as employed in Reference 8, although the truth is probably somewhere in between, closer to the current assumption. It is not possible, at the present time, to measure the velocity variation within the particles of the densely packed cloud. Furthermore, the kinetic energy of the ejecta is a small percentage of the initial energy, ranging from 7 to 15 percent in the present tests.

In the investigation of the first year, the kinetic energy of all fragments of sufficient size to be individually identified in the high-speed photographs was computed separately. This procedure was not followed in the present calculations because (a) the quantity of energy involved was small relative to the cloud energy, (b) significant inaccuracies in the magnitude calculated for the energy of these special fragments resulted from the lack of knowledge of the inclination of the trajectory with the normal to the specimen face, and (c) in some cases, it was difficult to identify a particular fragment in a sequence of frames. Thus, all ejecta was represented by a single distribution function.

The results of the investigation during the first year had provided a number of curves of particle size as a function of spatial distribution, that showed a Gaussian trend for the diorite; no further tests of this nature were considered necessary. On the other hand, the particle size distribution in each of the tests was electronically determined from the sampled regions. A typical photograph of the particles caught on the agar plate is reproduced in Figure 10 that shows the projected particle shapes of the ejecta; a reasonable approximation of these geometries appear to be circles and ellipses. The data for the number of particles vs. projected surface area obtained from the Quantimet samplings were fed into a computer program that scaled the mass of the particles collected to that of the crater using the same

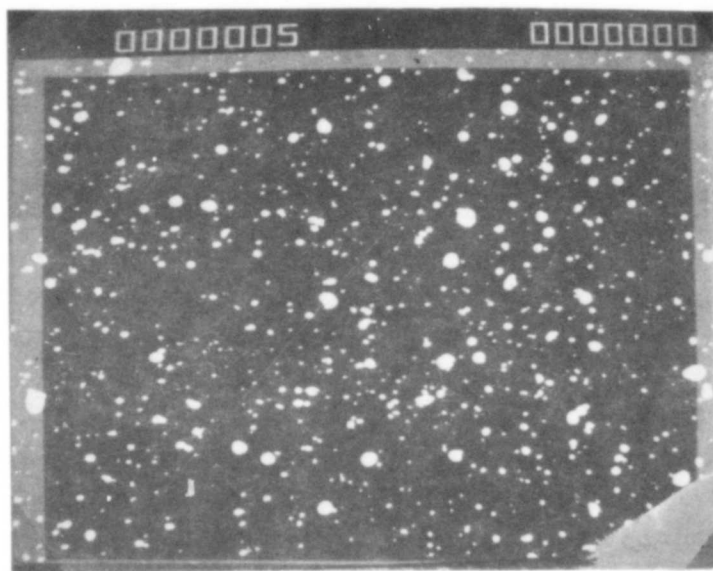


Fig. 10 - Typical Quantimet 720 Unit
Photographs; 2.5 mm x 3.2 mm Field of
View

particle size distribution as that experimentally determined. The output consisted of the number of particles, fraction of total particles, cumulative surface area and cumulative volume of the particles for each size range, based on two assumed simple particle geometries described by a single dimensional parameter. The shapes hypothesized were (a) an oblate spheroid with a series of ratios of minor to major axis lengths ranging from 0.1 to 1.0 in 0.1 increments, and (b) disks with a ratio of height to radius of either 0.3 or 5.0. These geometries conformed quite well to the observed projected shapes of Figure 10. A typical single test result for each of the three assumed shapes consisting of the two disks and a sphere is presented in Table 6. A histogram of the fraction of total particles derived by scaling the distribution obtained from the Quantimet readings for the particles actually collected to that corresponding to the entire crater volume as a function of square picture points is shown in Figure 11 for an assumed spherical particle shape. Square picture points represent the unit of viewing area in the Quantimet sampling that, for the present magnification, represent a domain $8.24 \times 10^{-4} \text{ mm}^2$. The cumulative information derived from Figure 11 has been replotted on a probabilistic scale, as indicated in Figure 12, yielding a good approximation to a normal fit. The same conclusion was drawn from the results of Reference 8 where the particles were collected on a gelatinous catcher plate and the size and spatial distributions were both evaluated. The logarithmic mean, $\text{Ln}\mu$, and standard deviation, σ , associated with a Gaussian description of the size distribution has been summarized in Table 7 as a function of input energy for three specific particle shapes, and the logarithmic mean has also been plotted in Figure 13. The discontinuities in this diagram are the result of the large variations found between samples, although the average can be readily drawn. From the data collected, there appears to be a trend towards decreasing particle size with increasing energy.

As may be noted from the summary for the diorite runs, Table 8, the ratio of recovered particle mass to crater mass ranged from about 40 to 80 percent. It was assumed in the previous calculations that this

TABLE 6a

GEOMETRICAL PROPERTIES OF THE EJECTA - DIORITE 180

PARTICLE SHAPE ASSUMED TO BE A DISK
HEIGHT = 5.0 RADIUS

AREA-CROSS SECTIONAL PIC.PIS	AREA-ONE PARTICLE SQ.MM	VOL.-ONE PARTICLE SQ.MM	NUMBER-OF PARTICLES	FRACTION PARTICLES	AREA-ALL PARTICLES SQ.MM	VOL.-ALL PARTICLES CU.MM
1.000E+01	3.660E-02	6.245E-04	1.461E+01	1.400E-02	5.345E-01	9.122E-03
2.000E+01	7.319E-02	1.766E-03	1.701E+02	1.630E-01	1.245E+01	3.004E-01
4.000E+01	1.464E-01	4.996E-03	1.744E+02	1.672E-01	2.554E+01	8.715E-01
8.000E+01	2.928E-01	1.413E-02	3.307E+02	3.170E-01	9.683E+01	4.674E+00
1.600E+02	5.855E-01	3.997E-02	1.492E+02	1.430E-01	8.736E+01	5.963E+00
3.200E+02	1.171E+00	1.130E-01	1.065E+02	1.040E-01	1.271E+02	1.227E+01
6.400E+02	2.360E+00	3.235E-01	6.980E+01	6.690E-02	1.648E+02	2.258E+01
1.300E+03	4.605E+00	8.980E-01	1.461E+01	1.400E-02	6.814E+01	1.313E+01
2.500E+03	9.149E+00	2.469E+00	6.469E+00	6.200E-03	5.916E+01	1.597E+01
5.000E+03	1.830E+01	6.982E+00	4.904E+00	4.700E-03	8.973E+01	3.424E+01
1.000E+04						
TOTAL (PART, FRAC, AREA, VOL)	1.043E+03	1.070E+00	7.316E+02	1.100E+02		

TABLE 6b

GEOMETRICAL PROPERTIES OF THE EJECTA - DIORITE 180

PARTICLE SHAPE ASSUMED TO BE A DISK
HEIGHT = 3/10 RADIUS

AREA-CROSS SECTIONAL PIC.FTS	AREA-ONE PARTICLE SQ.MM	VOL.-ONE PARTICLE SQ.MM	NUMBER OF PARTICLES	FRACTION PARTICLES	AREA-ALL PARTICLES SQ.MM	VOL.-ALL PARTICLES CU.MM
1.000E+01	3.029E-02	2.128E-04	4.287E+01	1.400E-02	1.298E+00	9.122E-03
2.000E+01	6.057E-02	6.019E-04	4.991E+02	1.630E-01	3.023E+01	3.004E-01
4.000E+01	1.211E-01	1.702E-03	5.120E+02	1.672E-01	6.202E+01	8.715E-01
8.000E+01	2.423E-01	4.015E-03	9.706E+02	3.170E-01	2.352E+02	4.674E+00
1.600E+02	4.846E-01	1.062E-02	4.379E+02	1.430E-01	2.122E+02	5.963E+00
3.200E+02	9.692E-01	3.052E-02	3.184E+02	1.040E-01	3.086E+02	1.227E+01
6.400E+02	1.953E+00	1.102E-01	2.048E+02	6.690E-02	4.001E+02	2.258E+01
1.300E+03	3.861E+00	3.063E-01	4.267E+01	1.400E-02	1.655E+02	1.313E+01
2.500E+03	7.572E+00	8.412E-01	1.898E+01	6.200E-03	1.437E+02	1.597E+01
5.000E+03	1.514E+01	2.579E+00	1.439E+01	4.700E-03	2.179E+02	3.424E+01
1.000E+04						
TOTAL (PART, FRAC, AREA, VOL)	3.062E+03	1.000E+00	1.777E+03	1.100E+02		

TABLE 6c

GEOMETRICAL PROPERTIES OF THE EJECTA - DIORITE 180

MINOR AXIS/MAJOR AXIS = 1.000

AREA-CROSS SECTIONAL PIC.PIS	AREA-ONE PARTICLE SQ.MM	VOL.-ONE PARTICLE SQ.MM	NUMBER OF PARTICLES	FRACTION PARTICLES	AREA-ALL PARTICLES SQ.MM	VOL.-ALL PARTICLES CU.MM
1.000E+01	4.659E-02	9.458E-04	9.645E+00	1.400E-02	4.494E-01	9.122E-03
2.000E+01	9.319E-02	2.675E-03	1.123E+02	1.630E-01	1.047E+01	3.004E-01
4.000E+01	1.864E-01	7.566E-03	1.152E+02	1.672E-01	2.147E+01	8.715E-01
8.000E+01	3.728E-01	2.140E-02	2.184E+02	3.170E-01	8.141E+01	4.674E+00
1.600E+02	7.455E-01	6.053E-02	9.852E+01	1.430E-01	7.345E+01	5.963E+00
3.200E+02	1.491E+00	1.712E-01	7.165E+01	1.040E-01	1.068E+02	1.227E+01
6.400E+02	3.005E+00	4.099E-01	4.609E+01	6.690E-02	1.385E+02	2.258E+01
1.300E+03	5.940E+00	1.361E+00	9.645E+00	1.400E-02	5.729E+01	1.313E+01
2.500E+03	1.165E+01	3.738E+00	4.271E+00	6.200E-03	4.976E+01	1.597E+01
5.000E+03	2.330E+01	1.057E+01	3.238E+00	4.700E-03	7.544E+01	3.424E+01
1.000E+04						
TOTAL (PART, FRACT, AREA, VOL)	6.089E+02	1.000E+00	6.151E+02	1.100E+02		

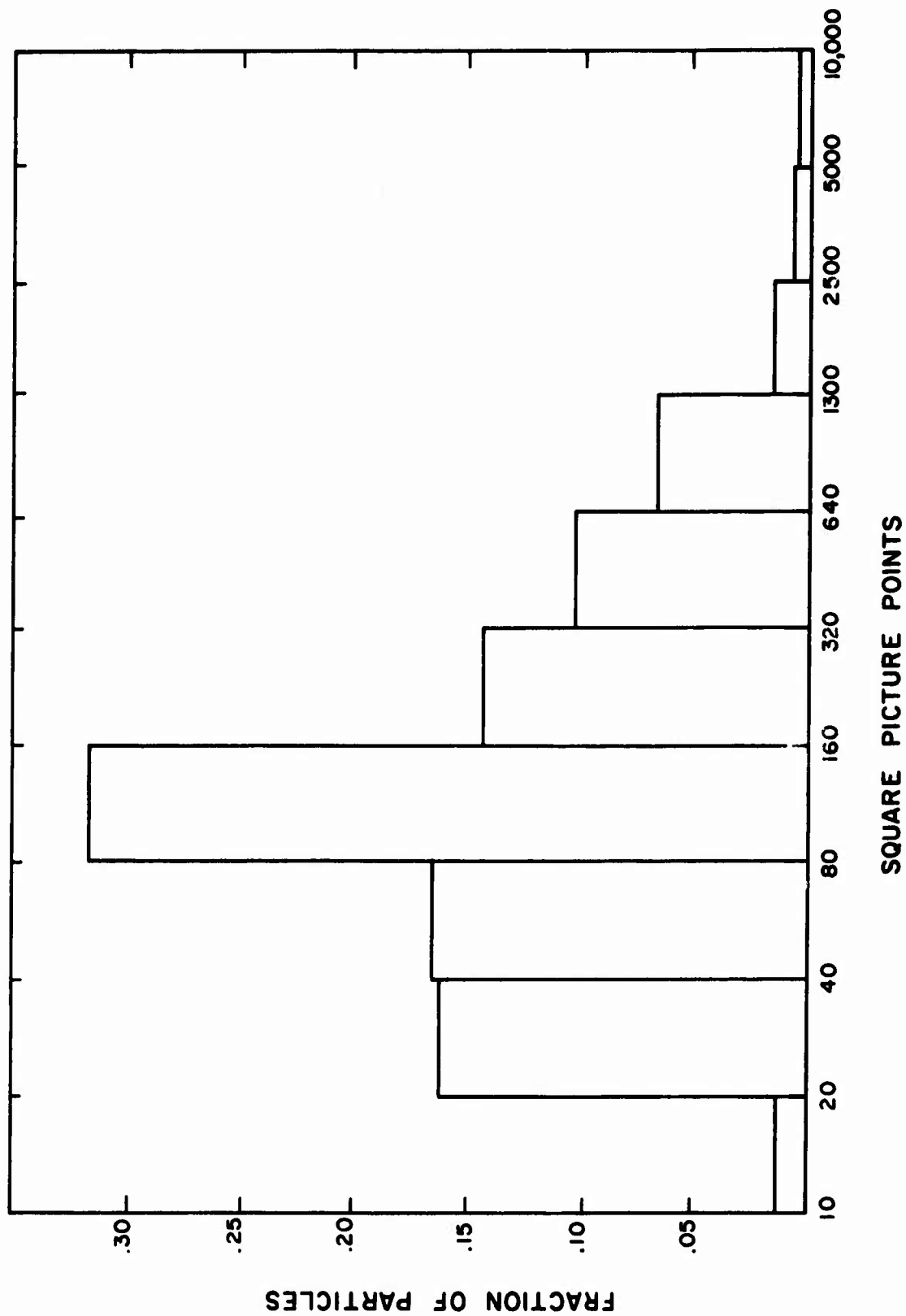


Fig. 11 - Histogram of the Fraction of Particles versus Particle Size for an Assumed Spherical Shape for Run D180

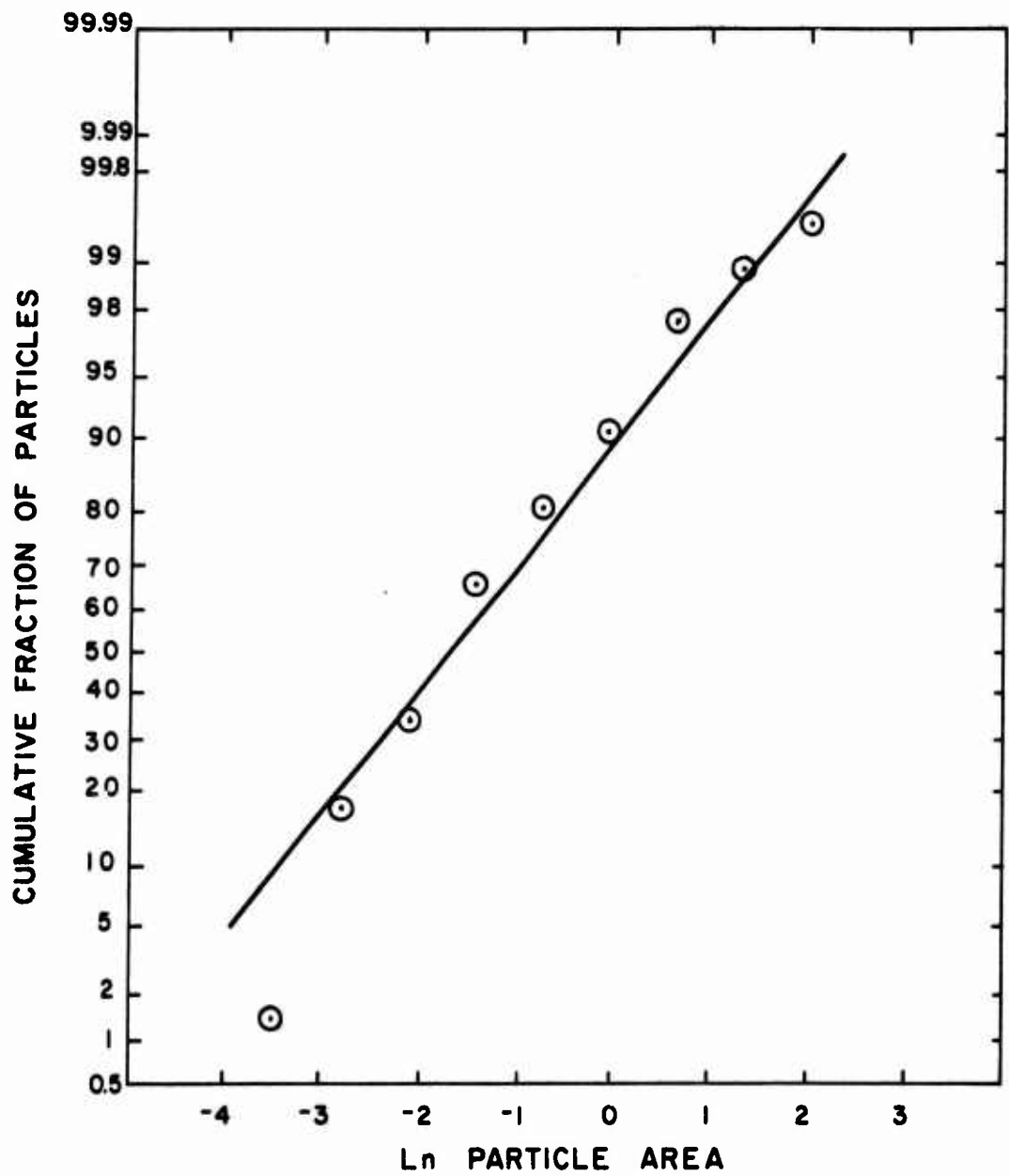
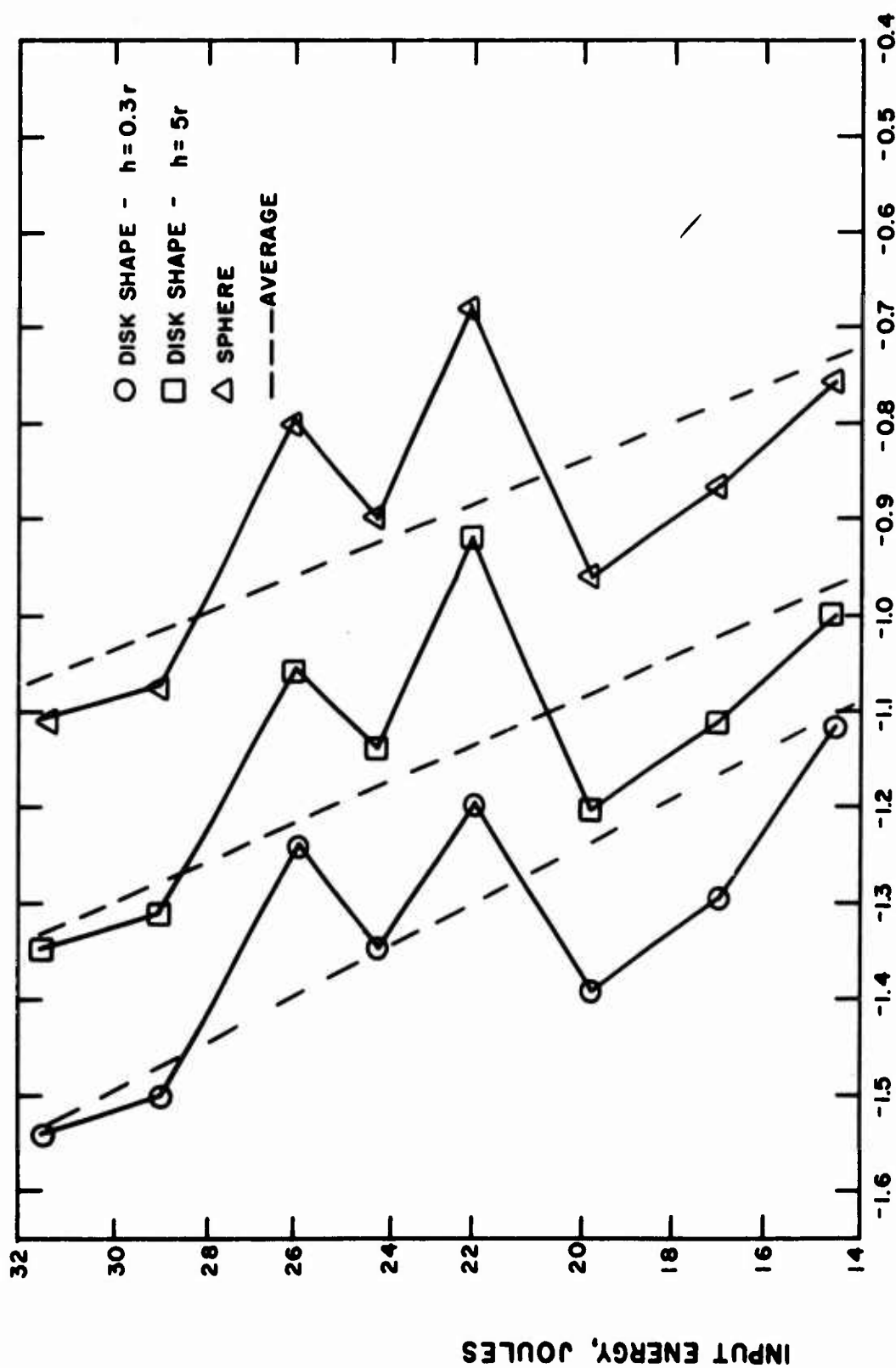


Fig. 12 - Probabilistic Ejecta Distribution for Run D180

TABLE 7. MEAN AND STANDARD DEVIATION OF EJECTA SURFACE AREAS FOR THREE PARTICLE SHAPES

Sample	Gross Energy, J	Sphere		Disk, h=0.3r		Disk, h=5r	
		Mean, μ , mm	Deviation, σ , mm ²	Mean μ , mm	Deviation σ , mm ²	Mean μ , mm ²	Deviation σ , mm ²
D100	14.5	0.469	± 4.14	0.305	± 4.14	0.368	± 4.14
D120	17.0	0.421	± 3.28	0.274	± 3.28	0.331	± 3.28
D140	19.8	0.383	± 3.22	0.249	± 3.22	0.301	± 3.22
D160	22.3	0.508	± 3.44	0.330	± 3.44	0.399	± 3.44
D180	24.3	0.408	± 3.08	0.260	± 3.08	0.321	± 3.08
D200	26.1	0.451	± 3.35	0.290	± 3.35	0.354	± 3.35
D220	29.0	0.343	± 3.54	0.223	± 3.54	0.269	± 3.54
D240	31.5	0.330	± 4.01	0.215	± 4.01	0.260	± 4.01



$\ln \mu$, \ln MEAN PARTICLE SIZE

Fig. 13 - Energy Input versus Mean Particle Size for Three Particle Shapes

TABLE 8. DIORITE TEST RESULTS

Data	Units	D 100	D 120	D 140	D 160	D 180	D 200	D 220	D 240
Gun Pressure	psi	100	120	140	160	180	200	220	240
Initial Projectile Velocity	m/s	(1) 167.1 (2) 178.0	181.0 180.0	195.0 150.0	206.0 192.0	213.4 197.0	224.0 197.0	236.0 229.0	246.0 231.0
Final Projectile Velocity(2)	m/s	~25.9	28.0	33.1	25.0	27.0	33.0	32.4	32.8
Initial Energy of Ball, E_{bi}	J	14.5	17.0	19.8	22.3	24.3	26.1	29.0	31.5
Final Energy of Ball, E_f	J	0.300	0.408	0.567	0.325	0.380	0.578	0.549	0.559
Wave Energy, E_w	J	0.955	1.077	2.490	1.296	1.087	0.674	2.503	2.052
Ejecta Energy, E_{ej}	J	1.013	2.391	2.280	3.610	2.884	4.416	4.540	2.075
Comminution Energy, E_{com}	J	12.2	13.1	14.5	17.1	19.9	20.4	21.4	26.8

(1) Photodiode velocity measurement

(2) High speed camera calculation

TABLE 8 (cont'd). DIORITE TEST RESULTS

Data	Units	D 100	D 120	D 140	D 160	D 180	D 200	D 220	D 240
$(E_{com}/E_{bi}) \times 100$, Per - Efficiency	cent	84.1	77.1	73.2	76.7	81.9	78.2	73.8	85.1
Crater Volume	mm ³	115	92	82	111	110	106	155	134
Maximum Diameter of Crater	mm	16.22	12.62	13.65	13.72	13.61	14.08	19.20	15.63
Minimum Diameter of Crater	mm	6.40	7.68	8.53	8.50	8.78	7.04	10.75	6.48
Maximum Depth of Crater	mm	2.12	2.00	1.65	2.13	2.15	2.34	2.46	2.24
Net Surface Area of Crater, A_c	mm ²	15.4	18.1	16.4	21.3	27.5	30.4	34.3	29.7
Area of Ejecta(3), A_{ej}	mm ²	1317	1466	1381	1713	1777	1585	2094	1601
Ejecta Mass, M_{ej}	grams	0.237	0.150	0.177	0.134	0.119	0.164	0.251	0.232

(3) Based on a spherical particle shape.

TABLE 8 (cont'd). DIORITE TEST RESULTS

Data	Units	D 100	D 120	D 140	D 160	D 180	D 200	D 220	D 240
Crater Mass, M_c	grams	0.308	0.246	0.218	0.296	0.293	0.283	0.414	0.358
Mass Scale Factor, M_c/M_{ej}	g/g	1.300	1.640	1.232	2.209	2.462	1.726	1.649	1.543

non-recovered mass followed the same size distribution as that collected in the catcher unit. This assumption is probably in error, since the fragments most likely to have escaped the measurement process were those at the extreme end of the distribution spectrum. The larger particles had the best chance to perforate the liner, while the smallest ones, amounting to dust, were most likely lost in the transfer operations. Thus, an appraisal of the effect of these losses on the actual particle size distribution would indicate that the mean value was probably not strongly affected, but that the deviation might be considerably larger and the distribution thus widened. The total ejecta surface area is most likely not changed a great deal by this increment in the distribution.

c. Wave Energy

In a previous parallel investigation, Reference [13], an estimate was given of the amount of energy in the hemispherical wave produced in a block of homogeneous, isotropic elastic material due to a prescribed time-dependent load applied over a small portion of the surface of the material. The values obtained were based on calculations of an exponentially decaying pressure input applied to the surface of a small spherical cavity on the inside of an infinite medium^[14] and a prescribed ratio of tangential to radial strain, assumed to be $1/2$. Surface strain gages provided the information for the value of peak radial strain that was taken to be the maximum pressure in the solution of the boundary value problem. The result indicated that the energy fraction consumed in the elastic wave amounted to from about 5 to 15 percent of the initial energy of the projectile. The present effort involves the measurement of both radial and tangential strains in the interior of the specimen and a more accurate analytical representation of the physical process in an attempt to obtain a better evaluation of the magnitude of this energy component.

The wave energy was calculated on the basis of the identical basic assumption as above of a perfectly spherical elastic transient emanating from the impact point through one-half of an infinite space

of density ρ . At any distance r from the contact location, the work done W by the pressure $-\sigma_{rr}$ on the internal hemispherical cavity is given by

$$W = -2\pi r^2 \int_0^\tau \sigma_{rr} \langle t \rangle \dot{u} \langle t \rangle dt \quad (5)$$

where u is the radial displacement, t is time measured from the start of the pulse at position r , τ is the pulse duration, and a superposed dot represents differentiation with respect to time. The radial stress σ_{rr} is given from Hooke's law as

$$\sigma_{rr} = (\lambda + 2G)\epsilon_{rr} + \lambda(\epsilon_{\theta\theta} + \epsilon_{\phi\phi}) \quad (6)$$

where the principal strains in directions r , θ and ϕ are given by ϵ_{rr} , $\epsilon_{\theta\theta}$, $\epsilon_{\phi\phi}$, and λ and G are the Lamé constants. For a symmetric wave, $\epsilon_{\theta\theta} = \epsilon_{\phi\phi}$ and hence

$$\sigma_{rr} \langle t \rangle = (\lambda + 2G)\epsilon_{rr} \langle t \rangle + 2\lambda\epsilon_{\theta\theta} \langle t \rangle \quad (7)$$

The particle velocity \dot{u} is then given by

$$\dot{u} = -c_D (\epsilon_{rr} + \epsilon_{\theta\theta}) \quad \text{where } c_D = \text{dilatational velocity} = \sqrt{\frac{\lambda+2G}{\rho}} \quad (8)$$

Substitution of Equations (7) and (8) in Equation (5) yields

$$W = 2\pi c_D^2 r^2 \left[(\lambda+2G) \int_0^\tau \epsilon_{rr}^2 \langle t \rangle dt + (3\lambda+2G) \int_0^\tau \epsilon_{rr} \langle t \rangle \epsilon_{\theta\theta} \langle t \rangle dt + 2\lambda \int_0^\tau \epsilon_{\theta\theta}^2 \langle t \rangle dt \right] \quad (9)$$

Since the radial and tangential strains were measured at different radii r and r^* , respectively, it was necessary to obtain their equivalent value at the same position. From the strain-displacement equations, this equivalence is given by

$$\epsilon_{\theta\theta} = (r^*/r)^2 \epsilon_{\theta\theta}^* \quad (10)$$

Substitution of this relation in Equation (9) yields the wave energy

$$E_w = W \text{ as } E_w = 2\pi c_D^2 r^2 \left[(\lambda+2G) \int_0^\tau \epsilon_{rr}^2 dt + (3\lambda+2G) (r^*/r)^2 \int_0^\tau \epsilon_{rr} \epsilon_{\theta\theta}^* dt + 2\lambda (r^*/r)^4 \int_0^\tau \epsilon_{\theta\theta}^{*2} dt \right] \quad (11)$$

in terms of the measured strains ϵ_{rr} and $\epsilon_{\theta\theta}^*$ whose location was given in Table 3 and whose history is exemplified in Figure 5.

A computer program was written to evaluate the integrals of Equation (11) using a trapezoidal rule.

A sample problem was constructed to test the accuracy of the program using assumed strain histories consistent with a spherical wave, given by

$$\begin{aligned} \epsilon_{\theta\theta} &= \begin{cases} (u_0/r) \sin \frac{\pi t}{\tau} & 0 \leq t \leq \tau \\ 0 & \text{otherwise} \end{cases} \\ \epsilon_{rr} &= \begin{cases} -(u_0/r) \left[\sin \frac{\pi t}{\tau} + (\pi r/c_D \tau) \cos \frac{\pi t}{\tau} \right] & 0 \leq t \leq \tau \\ 0 & \text{otherwise} \end{cases} \end{aligned} \quad (12)$$

Utilizing test data for u_0 and τ yielded computed values of E_w that were within 0.1 percent of the result obtained by exact integration.

For two of the tests, a malfunction occurred in the circuitry of tangential gage T2. This demanded a further investigation to determine whether the wave energy could be calculated from the history of only one radial gage with the necessity of additional assumptions. For an outward propagating spherical wave, starting at time $\bar{t} = 0$,

$$u = \left[F < \bar{t} - \frac{r}{c_D} > \right] / r \quad (13)$$

and since the strain-displacement equations are given by

$$\epsilon_{rr} = \frac{\partial u}{\partial r}, \quad \epsilon_{\theta\theta} = \epsilon_{\phi\phi} = \frac{u}{r} \quad (14)$$

it follows that

$$\epsilon_{rr} < \bar{t}, r > = -\frac{1}{r^2} F < \bar{t} - \frac{r}{c_D} > - \frac{1}{rc_D} F' < \bar{t} - \frac{r}{c_D} > \text{ and } \epsilon_{\theta\theta} < \bar{t}, r > = \frac{1}{r^2} F < \bar{t} - \frac{r}{c_D} > \quad (15)$$

where the prime denotes the derivative with respect to the argument.

Upon multiplication of Equation (15) by $-c_D/r$, use of the identity $\dot{\epsilon}_{\theta\theta} = \left[\dot{F} < \bar{t} - \frac{r}{c_D} > \right] / r^2 = \left[F' < \bar{t} - \frac{r}{c_D} > \right] / r^2$, and the strain-displacement relations, it follows that

$$\dot{\epsilon}_{\theta\theta} < t > + \frac{c_D}{r} \epsilon_{\theta\theta} < t > = -\frac{c_D}{r} \epsilon_{rr} < t > \quad (16)$$

Integrating this ordinary differential equation with the initial condition $\epsilon_{\theta\theta} < t > = 0$ for $t = 0$ (this is equivalent to $\epsilon_{\theta\theta} < \bar{t}, r > = 0$ for $\bar{t} \leq r/c_D$) yields

$$\epsilon_{\theta\theta} = \frac{c_D}{r} e^{-c_D t/r} \int_0^t \epsilon_{rr} < \tau > e^{c_D \tau/r} d\tau \quad 0 \leq \tau \leq t \quad (17)$$

As a check on the assumptions inherent in the derivation of Equation (17), the energies were calculated for all cases where both radial and tangential strain histories were available, and the results computed

by means of Equation (17) were compared with the data. Reasonable correspondence was obtained as indicated in Table 9 which exemplifies the wave energy calculations for Run D180.

The wave energy was computed for each test using gage R1 and the shifted value of gage T2 as the principal stations for the radial and tangential measurement, respectively. Since the tangential gage failed in runs D120 and D240, Equation (17) served as the replacement for these data.

Figure 14, which shows the actual and calculated values of for Run D180 indicates the nature of the discrepancies in the amplitude, rise time and duration of the two histories. Although these differences are not excessive and, as a result, it is not expected that significant changes in the wave energy would result from these variations, they do indicate that the basic assumptions of a spherically-symmetric wave in a homogeneous, isotropic elastic medium are not satisfied exactly in the present instance, as known a priori; however, these hypotheses do provide results of sufficient accuracy for the present purpose, particularly since the wave energy represents a relatively small portion of the impact energy.

d. Crater

As in the earlier work, crater topography measurements were executed by means of feeler gages; a typical contour map is presented in Figure 15 and the volume and surface area of the craters are summarized in Table 8. The crater contours ordinarily exhibited at least one axis of symmetry and a relatively smooth interior shape. The crater depth and the maximum crater diameter were approximately one-half and one projectile diameter, respectively, as was also observed previously^[8].

e. Cracks

Although inhomogeneities, previously existing cracks, stress concentrations and stored internal energy might alter the axial symmetry of the response of the rock sample to the central impact by the steel sphere, the influence of these factors cannot be quantitatively evaluated in the present or any foreseeable investigation. In consequence, as also somewhat reinforced by visual inspection on a diametral section of the damage pattern in the specimens, the extent of the crack system produced by the impact had to be assumed and for the sake of simplicity

TABLE 9a
STRAIN WAVE ANALYSIS
DIORITE 18F

DISTANCE TO RADIAL GAGE 17.980 MM
DISTANCE TO TANGENTIAL GAGE 37.030 MM

STRAIN WAVE ENERGY 1.087 JOULES

POINT	TIME X(E-6)	RADIAL X(E-6)	TANGEN. X(E-6)
1	0.	0.	0.
2	.29	3.00	-8.52
3	.57	7.99	-23.43
4	.86	9.99	-35.14
5	1.15	14.98	-42.68
6	1.44	19.98	-59.64
7	1.72	24.97	-83.07
8	2.01	34.96	-110.76
9	2.30	49.95	-146.97
10	2.58	69.93	-175.72
11	2.87	109.89	-202.35
12	3.16	179.82	-219.39
13	3.45	244.75	-244.95
14	3.73	304.69	-263.05
15	4.02	364.63	-274.77
16	4.31	424.57	-281.16
17	4.59	489.51	-284.35
18	4.88	559.44	-284.35
19	5.17	619.38	-282.22
20	5.46	679.32	-276.90
21	5.74	744.25	-270.51
22	6.03	809.19	-255.60
23	6.32	869.13	-239.62
24	6.61	929.07	-225.78
25	6.89	979.02	-211.93
26	7.18	1043.95	-202.35
27	7.47	1098.90	-184.24
28	7.75	1118.88	-174.66
29	8.04	1143.85	-166.14
30	8.33	1148.85	-157.62
31	8.62	1143.85	-153.36
32	8.90	1128.87	-146.97
33	9.19	1098.90	-138.45
34	9.48	1053.94	-130.99
35	9.76	1023.97	-127.80
36	10.05	989.01	-117.15
37	10.34	964.03	-112.89
38	10.63	939.06	-106.50
39	10.91	899.10	-101.17
40	11.20	864.13	-95.85

TABLE 9a (cont'd)

41	11.49	629.17	-92.65
42	11.77	789.21	-91.59
43	12.06	744.25	-92.65
44	12.35	719.28	-93.72
45	12.64	689.31	-95.85
46	12.92	669.33	-97.98
47	13.21	654.34	-97.98
48	13.50	634.36	-96.91
49	13.78	614.38	-93.72
50	14.07	589.41	-88.39
51	14.36	564.43	-82.00
52	14.65	539.46	-76.68
53	14.93	514.48	-72.42
54	15.22	499.50	-69.22
55	15.51	474.52	-68.16
56	15.79	449.55	-66.03
57	16.08	429.57	-63.90
58	16.37	414.58	-61.77
59	16.66	399.60	-58.57
60	16.94	384.61	-54.31
61	17.23	374.62	-50.05
62	17.52	354.64	-41.53
63	17.81	339.66	-38.34
64	18.09	309.69	-31.95
65	18.38	284.71	-26.62
66	18.67	254.74	-18.10
67	18.95	239.76	-12.78
68	19.24	219.78	-5.32
69	19.53	189.81	0.
70	19.82	164.83	0.
71	20.10	144.85	0.
72	20.39	119.88	0.
73	20.68	99.90	0.
74	20.96	79.92	0.
75	21.25	59.94	0.
76	21.54	39.96	0.
77	21.83	24.97	0.
78	22.11	9.99	0.
79	22.40	0.	0.

TABLE 9b

STRAIN WAVE ANALYSIS
DIORITE 180

DISTANCE TO RADIAL GAGE 17.980 MM
DISTANCE TO TANGENTIAL GAGE 17.980 MM

STRAIN WAVE ENERGY .833 JOULES

POINT	TIME X(E-6)	RADIAL X(E-6)	TANGEN. X(E-6)
1	0.	0.	0.
2	.29	3.88	-.10
3	.57	7.99	-.45
4	.86	9.99	-1.88
5	1.15	14.98	-1.74
6	1.44	19.98	-2.75
7	1.72	24.97	-4.82
8	2.01	34.96	-5.69
9	2.30	49.95	-8.86
10	2.58	69.93	-11.48
11	2.87	109.89	-16.47
12	3.16	179.82	-24.76
13	3.45	244.75	-36.84
14	3.73	304.69	-52.13
15	4.02	364.63	-70.28
16	4.31	424.57	-91.18
17	4.59	489.51	-114.68
18	4.88	559.44	-143.91
19	5.17	619.38	-169.68
20	5.46	679.32	-208.45
21	5.74	744.25	-233.26
22	6.03	809.19	-268.12
23	6.32	869.13	-304.74
24	6.61	929.07	-342.86
25	6.89	979.02	-382.04
26	7.18	1043.95	-422.41
27	7.47	1098.90	-464.82
28	7.75	1118.88	-505.33
29	8.04	1143.85	-545.44
30	8.33	1148.85	-583.92
31	8.62	1143.85	-619.93
32	8.90	1128.87	-652.98
33	9.19	1098.90	-682.47
34	9.48	1053.94	-787.65
35	9.76	1023.97	-728.85
36	10.05	989.01	-746.60
37	10.34	964.03	-761.31
38	10.63	939.06	-773.47
39	10.91	899.10	-782.77
40	11.20	864.13	-789.86

TABLE 9b (cont'd)

41	11.49	629.17	-792.75
42	11.77	789.21	-793.77
43	12.06	744.25	-792.01
44	12.35	719.28	-788.15
45	12.64	689.31	-782.77
46	12.92	669.33	-776.14
47	13.21	654.34	-768.83
48	13.50	634.36	-768.86
49	13.78	614.38	-752.12
50	14.07	589.41	-742.50
51	14.36	564.43	-731.89
52	14.65	539.46	-720.36
53	14.93	514.48	-707.97
54	15.22	499.50	-695.11
55	15.51	474.52	-681.78
56	15.79	449.55	-667.70
57	16.08	429.57	-653.89
58	16.37	414.58	-638.31
59	16.66	399.61	-623.51
60	16.94	384.61	-608.69
61	17.23	374.62	-594.03
62	17.52	354.64	-579.34
63	17.81	339.66	-564.48
64	18.09	309.69	-549.11
65	18.38	284.71	-532.97
66	18.67	254.74	-516.10
67	18.95	239.76	-498.89
68	19.24	219.78	-481.65
69	19.53	189.81	-463.91
70	19.82	164.83	-445.55
71	20.10	144.85	-426.93
72	20.39	119.88	-408.06
73	20.68	99.90	-388.96
74	20.96	79.92	-369.81
75	21.25	59.94	-350.60
76	21.54	39.96	-331.35
77	21.83	24.97	-312.21
78	22.11	9.99	-293.33
79	22.40	0.	-274.87

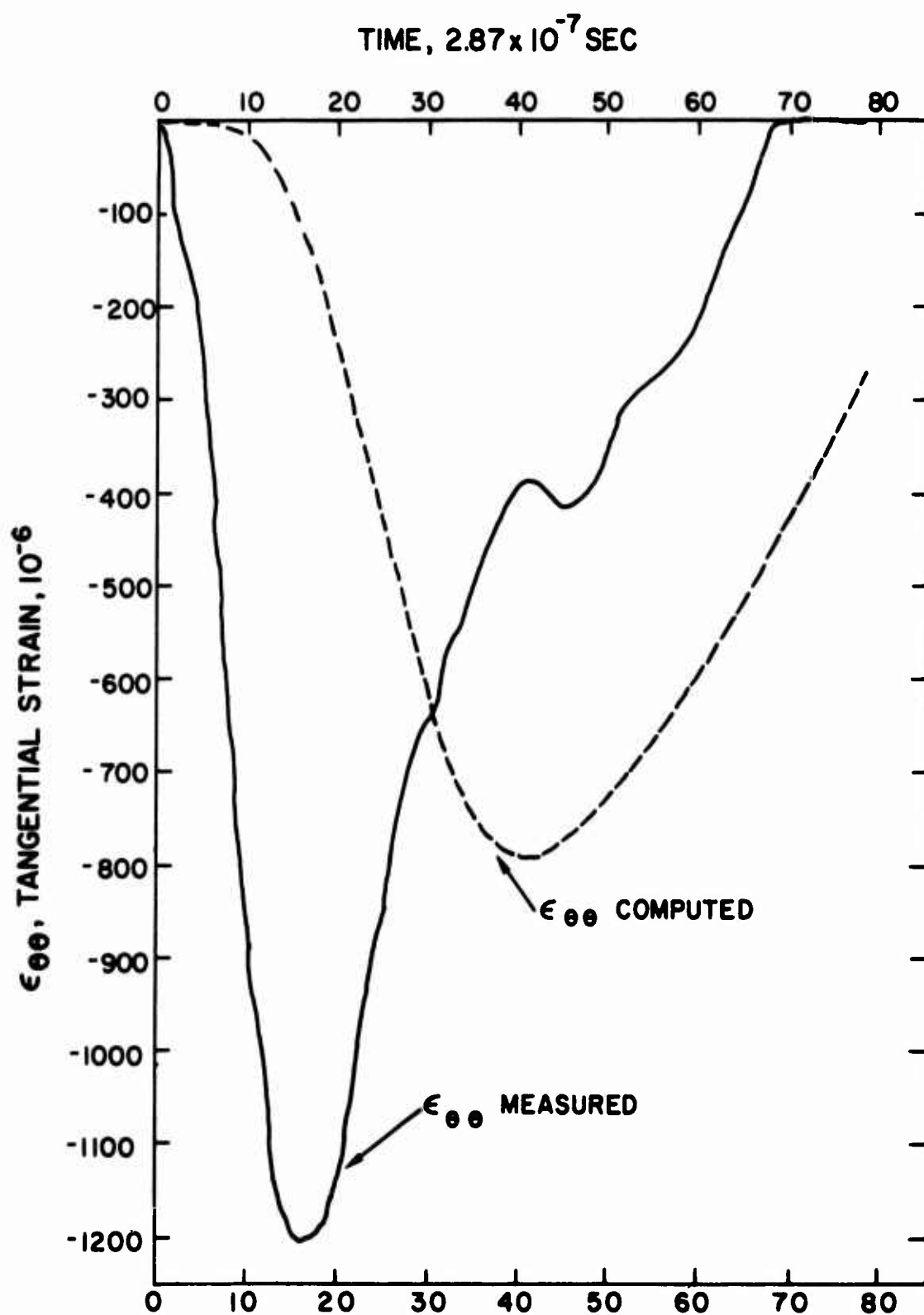


Fig. 14 - Comparison of Measured and Predicted Tangential Strain Histories for Run 180

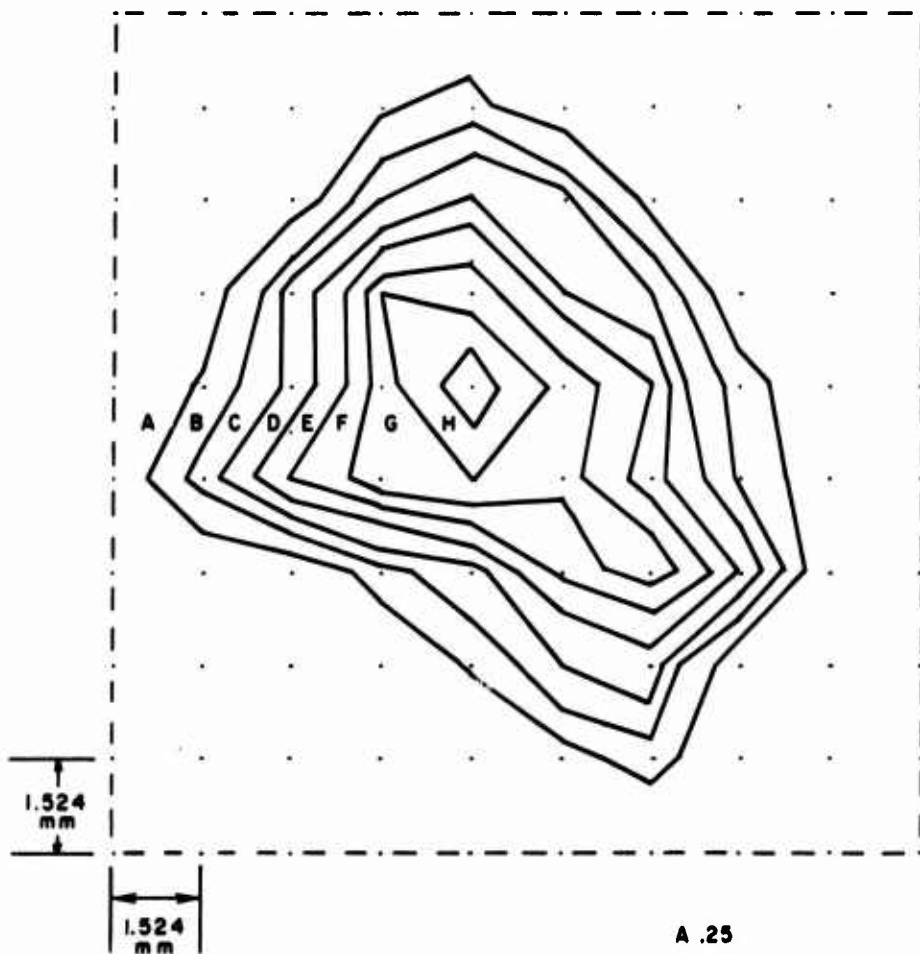


Fig. 15 - Typical Contour Map of a
Diorite Crater, Run D180

A .25
B .50
C .75
D 1.00
E 1.25
F 1.50
G 1.75
H 2.00

was taken to be symmetric about the impact axis, forming surfaces of revolution. A computer program, whose listing is given in Appendix A, was developed that calculated the area associated with these new surfaces, the length and angular orientation of each crack and their total number based on an input that stipulated the end points of the cracks with respect to a coordinate system centered at the point of impact; it was assumed that the cracks on the diametral surface were straight lines. These inputs were also employed to generate a computer plot of the diametral section, such as shown in a five-fold enlargement in Figure 16; the corresponding 13.7 times photographic enlargement of the actual specimen is presented in Figure 7. The scheme of the machined sections is also included in this figure.

The crack surface so computed cannot distinguish between that produced by the impact and that preexisting. In order to attempt to account for the initially present crack surfaces, the computed areas were adjusted on the basis of a crack network sampled in two selected specimens D120 and D220 at regions A or C which were so remote from the impact point that they were believed not to have been affected in any way by the contact phenomenon and were thus representative of the virgin state. The crack surface per unit volume believed to exist originally throughout the specimen was computed both on the basis that the axis of symmetry passed through the center of the region examined, and on the basis of an isotropic crack pattern using the average value of the cracks for the two specimens D120 and D220. The net crack surface due to the impact was taken as the difference between these values; it is shown in Table 10 for both methods of calculation. It is clear, in view of the negative crack areas calculated in this fashion, that the procedure adopted is highly questionable, even on an average basis. Apparently, individual variations in the initial crack configurations grossly overshadow that generated by the impact as was also confirmed by visual inspection of all samples tested, and average values simply cannot be applied to the present situation.

CRACK ANALYSIS DIORITE 180

COMMINUTION ENERGY (JOULES)
19.8

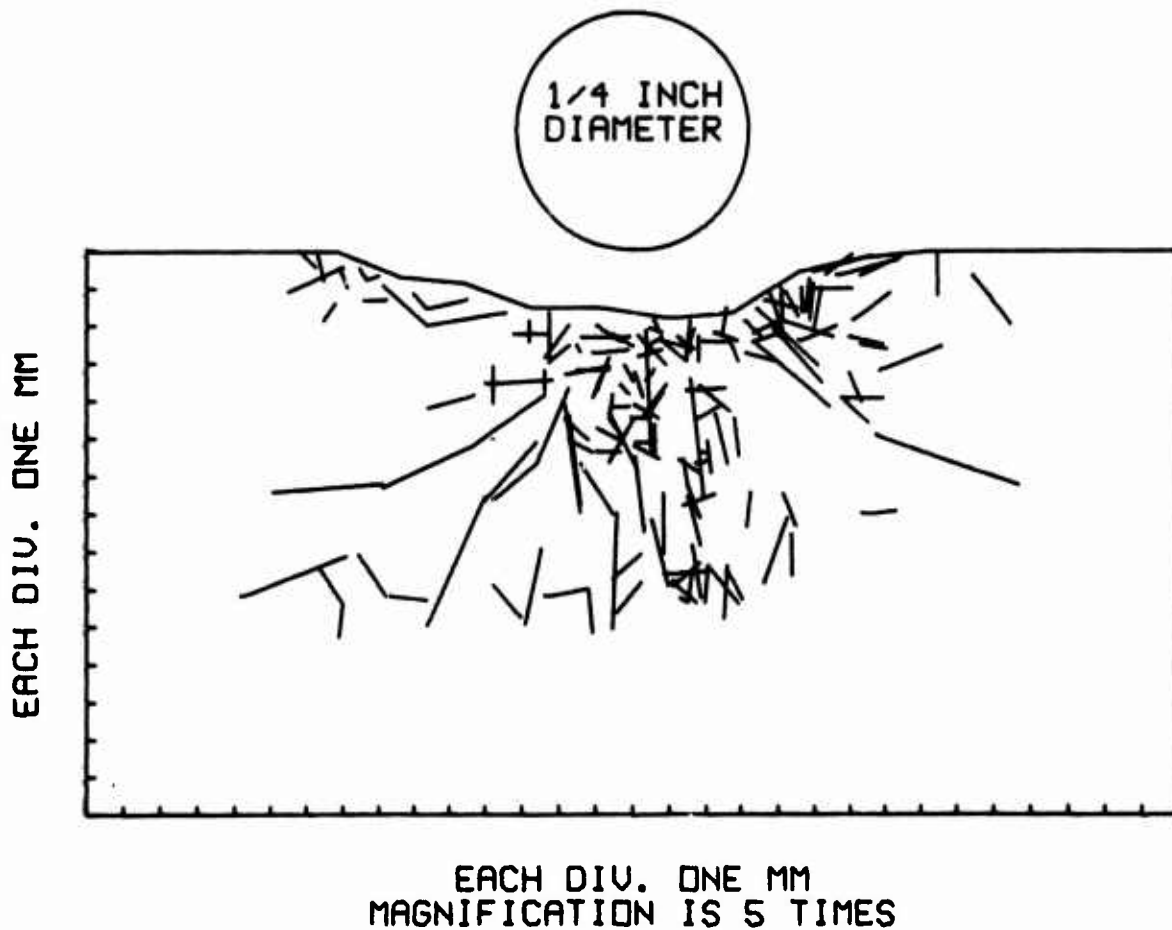


Fig. 16 - Typical CALCOMP Plot Approximating
the Cross-sectional Crack Distribution

Another attempt was made to overcome these individual variations. The entire central diametral section of the specimens, domain B, was covered with the dye penetrant and the developer was applied. This yielded disjointed regions of visible crack damage, as shown in Figure 17. The crack network in a subregion of the damaged domain, a distance of at least one diameter away from the crater, was examined and the ratio of the dyed (cracked) to the total surface area within that domain of scrutiny was determined. This area factor was now applied to adjust the initially assumed preexisting crack distribution, determined on the basis of the average of samples D120 and D220, to conform to the cracks present in the actual cross section of each test specimen by multiplying this average crack surface area by the quotient of the ratios of dyed to total areas of the actual and the two selected specimens. The result was considered to be the estimate of the preexisting damage in each of the test specimens, and is also shown in Table 10. A net crack surface generated by the impact based on this preexisting crack computation is also included. Finally, a calculation is summarized in the table which bases the preexisting crack surface area on the total crack length per surface area found in the region under examination; this quantity can readily be related to crack surface per unit volume. As may be seen, all of these approaches yielded negative crack surface estimates produced by the impacts for at least some of the specimens, a situation that is considered to be phenomenologically unrealistic. This situation exists even when the procedure is applied to the same central section of the selected samples whose crack area several diameters away from the impact region was employed as the standard for the fabric of the virgin specimen.

Since it is not possible to determine the extent of preexisting cracks prior to the test without destroying the specimen, it is either necessary to utilize statistical results that are physically acceptable, even when some of the ingredient information violates a reasonable interpretation of the phenomenon, or else be satisfied with bounds on the new surface generated that ignores the crack sampling outside the impact zone.



(a)



(b)

Fig. 17 - Photograph of
Typical Dyed Samples

(a) Run D120

(b) Run D220

TABLE 10. CRACK SURFACE AREA BASED ON VARIOUS ASSUMPTIONS

Run	Total Crack Surface Area, A_t , mm ²	Adjusted Area $A_{adj}(1)$, mm ² (4)	Adjusted Area $A_{adj}(2)$, mm ² (2)	Adjusted Area $A_{adj}(3)$, mm ² (3)
D 120 A	5469	5110	4926	1694
D 220 C	7367	7916	8213	3042
D 100	5311	9421	17108	5812
D 120	5584	3324	3198	6455
D 140	8582	10800	22460	6471
D 160	4571	947	205	4224
D 180	3960	3020	1485	6426
D 200	6036	1075	224	6433
D 220	5805	5953	6176	6354
D 240	7821	3703	2118	7298

(1) Remote measurement

(2) Remote measurement scaled by dye penetrant ratio

(3) Remote measurement scaled by crack length ratio

(4) Adjusted areas for all runs involve the average of D120 A and D 220 C areas.

TABLE 10 (cont'd). CRACK SURFACE AREA BASED ON VARIOUS ASSUMPTIONS

Run	Net Area $A_{Cr(1)}$, mm ² (5)	Net Area $A_{Cr(2)}$, mm ²	Net Area $A_{Cr(3)}$, mm ²	Total Length, mm	Length Per Viewing Area, mm ⁻¹
D 120 A	359	543	3775	176.1	.958
D 220 C	-550	-845	4325	171.6	0.672
D 100	-4110	-11797	-500	161.5	0.919
D 120	2260	2386	-871	237.5	1.194
D 140	-2218	-13874	2110	288.6	1.489
D 160	3624	4366	348	167.5	1.101
D 180	946	2475	-2466	177.6	0.829
D 200	901	5812	-396	202.6	1.005
D 220	-148	-371	-549	207.2	1.015
D 240	4118	5703	524	297.3	1.163

(1) Remote measurement

(2) Remote measurement scaled by dye penetrant ratio

(3) Remote measurement scaled by crack length ratio

(5) Net area (1) = $A_{Cr}^{(1)} = A_t - A_{adj}^{(1)}$, i = 1, 2, 3

The average of all positive and negative generated crack surfaces based on the dyeing procedure and application of the area factors was evaluated as 1490 mm^2 for the impact of a 1/4 inch diameter steel sphere in the velocity range from 169 to 246 m/sec; individual variations within this span were completely obscured by the differences within the samples supplied.

In view of the above considerations, the energy required to produce unit new surface will be computed on the following bases:

(a) All cracks located in the central diametral region that extended virtually to the edge of segment B of the specimens were considered to be produced by the impact, (b) A net crack surface based on the average new surface considered to be produced, amounting to 1490 mm^2 was incorporated in addition to the ejecta and net crater surfaces, and (c) All observed cracks were assumed to be preexisting. This information is compiled in Table 11, and is the energy of comminution required to produce new surface area based on the hypotheses indicated. Obviously, the scheme adopted here is such that the magnitude of this quantity increases from assumption (a) to assumption (c). For the range investigated, the energy per unit new surface generated differed by a factor of 2 within a given hypothesis, and exhibited an average value of 2.25×10^{-3} , about 6×10^{-3} and approximately $11 \times 10^{-3} \text{ J/mm}^2$ for cases (a), (b) and (c), respectively. The comminution efficiency, i.e. the fraction of initial kinetic energy utilized for the fragmentation process, can be noted in Table 8 to be of the order of 70 to 85 percent and to be essentially independent of initial projectile energy for the range of values employed in the present investigation.

f. Relation of Results of Comminution Theories

A characteristic particle size for the ejecta was chosen for each test as the mean value of the normal distribution, i.e. μ , for purposes of comparison with the comminution theories of Kick, Bond and Rittinger. The characteristic dimension of the specimen, to which the above was to be compared, was chosen as the magnitude of the vector resultant of the crater radius and depth. Table 12 contains the particle

TABLE 11. COMMINATION ENERGY PER UNIT OF NEW SURFACE AREA

Run	Total Area $A_t(a)$ mm ²	(1), (2) Total Area $A_t(b)$ mm ²	(3) Total Area $A_t(c)$ mm ²	(4) Total Area $A_t(c)$ mm ²	Comminution Energy, E_c , J	$E_c/A_t(a)$ 10 ⁻³ J/mm ²	$E_c/A_t(b)$ 10 ⁻³ J/mm ²	$E_c/A_t(c)$ 10 ⁻³ J/mm ²
D 100	6663	2823	1332	1332	12.2	1.84	4.33	9.16
D 120	7068	2975	1484	1484	13.1	1.85	4.40	8.83
D 140	9979	2888	1397	1397	14.5	1.45	5.02	10.40
D 160	6305	3225	1734	1734	17.1	2.71	5.30	9.86
D 180	5765	3296	1805	1805	19.9	3.45	6.04	11.02
D 200	7651	3106	1615	1615	20.4	2.67	6.57	12.60
D 220	7933	3619	2128	2128	21.4	2.70	5.91	10.06
D 240	9452	3122	1631	1631	26.8	2.84	8.58	16.43

(1) Total Area, $A_t = A_{cr} + A_{ej} + A_i$.

= Crater Area and Ejecta area for spherical particle assumption and area of internal cracks.

(2) Hypothesis (a), all cracks produced by impact

(3) Hypothesis (b), Net Crack Area = 1491 mm²

(4) Hypothesis (c), all cracks are pre-existing

TABLE 12. COMMINUTION CONSTANTS BASED ON QUASISTATIC THEORIES

Run	Characteristic Particle Size, L_2 , mm	Characteristic Initial Size L_1 , mm	Comminution Energy, E_C , J	Kick's Constant, C_k , J	Rittinger's Constant, C_R (2) $\times 10^{-2}$, J/mm	Bond's Constant, C_B (3) J/mm	Initial Crater(4) Mass Surface Area, mm^2
D 100	0.3863	8.3825	12.2	3.93	-4.572	-0.776	265.1
D 120	0.3612	6.6194	13.1	4.47	-6.040	-0.926	215.5
D 140	0.3493	7.0216	14.5	4.73	-6.320	-0.987	225.0
D 160	0.4021	7.1831	17.1	5.83	-6.520	-1.094	258.2
D 180	0.3605	7.1366	19.9	6.63	-9.304	-1.418	213.3
D 200	0.3787	7.4187	20.4	6.82	-8.397	-1.363	242.2
D 220	0.3303	9.9102	21.4	6.20	-5.919	-1.153	356.8
D 240	0.3243	8.1297	26.8	8.26	-8.972	-1.597	296.8

(1) For C_k , L_1 , L_2 are given above.

(2) For C_R , $1/L_1$ = initial crater mass surface area, $1/L_2$ = area of mean particle.

(3) For C_B , same as (2).

(4) Surface area of crater mass if ejected as a single chunk.

size, energy of comminution E_{com} and the constants C_k , C_r and C_b predicted from the Kick, Rittinger and Bond equations, respectively, given by

$$E = C_k \ln \left[L_1/L_2 \right] \quad (18) \text{ Kick}$$

$$E = C_r \ln \left[\frac{1}{L_2} - \frac{1}{L_1} \right] \quad (19) \text{ Rittinger}$$

$$E = 2C_b \left[\frac{1}{\sqrt{L_2}} \left(1 - \frac{1}{\sqrt{L_1/L_2}} \right) \right] \quad (20) \text{ Bond}$$

where L_1 and L_2 are the characteristic initial and final dimensions (length, area, or volume) and E is the energy of comminution. Although the magnitudes of these empirical constants have been determined for the present series of experiments, based on a scale involving a length dimension, and appear to increase with increasing input energy, the intent of the equations (18) to (20) was to utilize ratios of either volume or surface area rather than length, and thus a difference in the numerical results involving one or even more orders of magnitude might occur. Furthermore, since the block size for these equations was presumed to be semi-infinite, the initial value of the constants is based on an artificially selected magnitude. Since, furthermore, the relations were designed for applications involving crushing and grinding of a large mass into many smaller parts under quasi-static loading, it is likely that the present results utilizing these empirical relations cannot be extrapolated to other impact situations.

However, it was found that the mean particle size tends to decrease with increasing impact energy, as might be expected. Although the conservation of mass dictates that this size dimension must approach a lower limit, the present range of tests is insufficient to provide this information.

2. Shale

a. Ejecta

Since the earlier tests at comparable impact velocities indicated that minimal quantities of ejecta were produced in the shale specimens, only a few of the experiments conducted during the second year of operation were photographed, with a typical result shown in Figure 18. The cloud formation is distinctively different, forming a

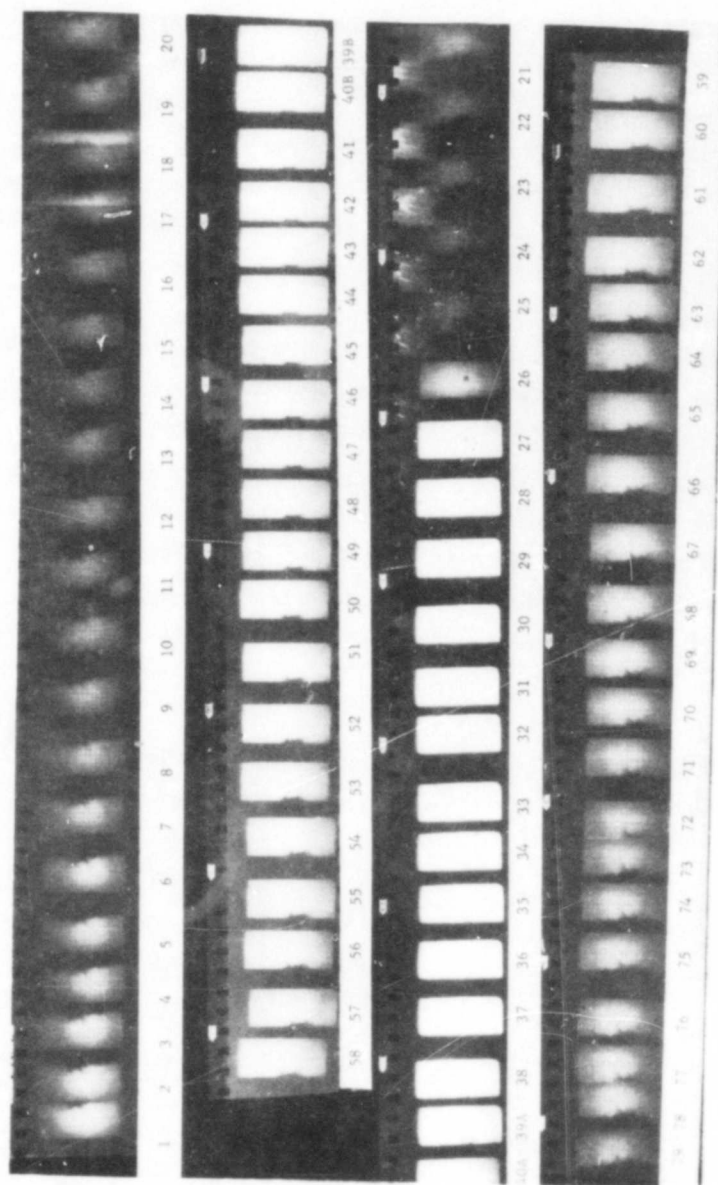


Fig. 18 - Film History of a
Typical Shale Test
Run S 40

thin sheaf rather than a relatively dense conical shell. It was found in the present tests that both the velocity of the fastest particles and the total mass of the ejecta were of the order of 1/10 that of the striking sphere; thus, the total energy of the ejecta amounted to no more than approximately 0.1 percent of the striking energy. In all photographs, the rebound trajectory of the striker was obscured by the ejecta cloud, but the terminal location of the ball in the catcher tank clearly indicated a negligible rebound velocity.

b. Dynamic Penetration

A summary of the penetration results due to the impact of the steel sphere on the shale specimens is presented in Table 13. Recalling the appearance of the penetration configuration as a cylindrical hole with a hemispherical bottom, with either very small or no dish around the entrance, it is possible to attempt to model the compaction phenomenon as a rigid projectile of mass m in entering a linearly viscous medium characterized by constant c , neglecting elastic compression rebound, ejecta and wave phenomena. The equation for this simple model is

$$m\ddot{x} + c\dot{x} = 0 \quad (21)$$

where x is the penetration. The energy absorbed by the viscous forces is then equal to the initial kinetic energy of the striker and is given by

$$E = -\int_0^P c\dot{x} dx \quad (22)$$

where P is the maximum penetration depth. The equation of motion has the general solution

$$x = x_0 e^{-ct/m} + C_0 \quad (23)$$

where the constants of integration, x_0 and C_0 , are evaluated from the conditions

$$t = 0, x = 0, \dot{x} = v_0 \quad \text{and} \quad t = \infty, x = P, \dot{x} = 0 \quad (24)$$

Upon substitution in Equation (23), the viscous constant c can be evaluated as

$$c = mv_0/P \quad (25)$$

TABLE 13. DYNAMIC SHALE PENETRATION DATA FOR A ¼-IN. DIAMETER STEEL SPHERE

Shale ^{(1), (2)}	P, Penetration Depth, mm	v, Velocity m/s	E, Energy, J	P/mv mm/g-m/s	$\frac{P^2}{E}$ mm ² /J
S20	1.74	51	1.4	.0341	2.163
S40	3.53	107	6.0	.0330	2.077
S60	4.32	131	8.9	.0330	2.097
S80	5.08	152	12.0	.0334	2.151
S100	5.43	169	14.9	.0316	1.979
S120	5.68	181	16.9	.0314	1.909
S140	5.94	194	19.4	.0306	1.819
S160	6.53	205	22.2	.0319	1.921
S180	7.06	213	23.7	.0331	2.103
S200	7.23	227	26.7	.0319	1.958
S220	7.98	235	28.8	.0340	2.211
S240	8.12	242	30.4	.0336	2.161
A9	31.75	852	378	.0373	2.667
A10	31.75	881	404	.0360	2.495
A11	31.75	570.59	169.30	.0535	5.958
A12	88.90	1718	1535	.0517	5.149
A13	29.46	512	136	.0575	6.382
A14	12.45	342	153	.0364	1.013
A15	32.00	896	417	.0357	2.456
A16	29.21	563	165	.0519	5.171
A17	29.21	567	167	.0515	5.109
A18	26.42	569	168	.0464	4.155
A19	24.89	554	160	.0449	3.872
A20	29.97	608.69	192.66	0.0473	4.663
A21	25.40	685	244	.0371	2.644
A22	25.40	591.01	181.63	0.0413	3.552
A23	22.10	497	128	.0445	3.816
A24	38.35	945.18	464.55	0.0390	3.166

TABLE 13 (cont'd). DYNAMIC SHALE PENETRATION DATA FOR A 1/2-IN. DIAMETER STEEL SPHERE

Shale (1), (2)	P, Penetration Depth, mm	v, Velocity m/s	E, Energy, J	P/mv mm/g-m/s	P ² /E mm ² /J
A25	39.12	966	485	.0405	3.160
A26	62.23	965.61	484.85	0.0620	7.987
A27	54.36	2487.17	3216.72	0.0210	0.918
A28	60.45	1501	1172	.0403	3.118
A29	17.02	537	150	.0317	1.931
A30	16.00	477	118	.0335	2.169
A31	44.45	939	458	.0473	4.314
A32	47.42	974	493	.0436	4.561
A33	16.00	527	144	.0304	1.778
A35	14.99	537	150	.0279	1.498
A36	63.50	1601	1333	.0397	3.025
A37	63.50	1618	1361	.0392	2.963
A38	37.34	843	370	.0443	3.768
A39	38.35	875	398	.0438	3.695
A40	20.32	502	131	.0405	3.152
A41	20.07	550	157	.0365	2.566
A42	14.99	449	105	.0334	2.148
A43 ³	64.008	1603.55	1337.12	0.0384	3.064
A45	78.99	1609	1346	.0491	4.612
A46 ³	39.878	874.78	397.92	0.0438	3.996

(1) S refers to tests conducted at the University of California, Berkeley

(2) A refers to tests conducted at the Naval Weapons Center, China Lake, California.

Actual integration of the energy equation (22) yields

$$E = (1/2)mv_o^2 \quad (26)$$

as expected, and substitution for v_o yields

$$(1/2)mv_o^2 = Q P^2 \quad \text{where} \quad Q = c^2/2m \quad (27)$$

The calculated values of Q and c for each test are reproduced in Table 13, their average being 0.489 J/mm^2 and 30.3 kg/sec , respectively, with very little scatter. It is expected that significant deviations will occur in this model when the initial velocity is so low that a penetration depth of at least one projectile radius is not obtained, nor under circumstances of high initial velocities when ejecta formation, gross cracking of the sample, and even backward spall are in evidence.

In Reference [8], a post mortem section of a 5-1/2 inch thick shale sample with a diameter of 5-1/2 inch, encased in plaster of Paris as in the current tests, struck by a 1/4 inch diameter steel sphere at a velocity of 5300 ft/sec was exhibited; the hole had been filled with a glue prior to sectioning. In this photograph reproduced in Figure 19, the hole appears as a truncated cone with a small cone angle and a dish at the entrance region; the projectile was embedded at the tip of this cone whose diameter was slightly smaller than that of the sphere, indicating some recovery of the compacted material. The discolored zone appearing as a bell-like shape around the hole is not necessarily an indication of the compacted region, as it may represent the extent of the glue penetration. The marked difference in appearance between this photograph and the shale crater produced at considerably lower velocities indicates the difference in the penetration patterns occurring in differing velocity regimes.

c. Quasi-static Tests

The results of the tests on the Instron machine are summarized in Table 14. Significant scatter and no consistency with respect to rate was obtained in the measured energy required to produce a given indentation under identical velocities of penetration; however, the data indicates a drastically greater energy requirement for a given depth of

TABLE 14. QUASISTATIC PENETRATION TESTS ON SHALE

		P, Penetration Depth, mm										
		0.5	1.0	1.5	2.0	2.5	3.0	3.5	4.0	4.5	5.0	5.5
Instron 1												
Rate: 5.08($\frac{\text{mm}}{\text{min}}$)												
E, J		.069	.276	.611	1.071	1.652	2.320	2.992	3.700	4.459	5.279	
D ² /E		3.623	3.623	3.682	3.735	3.783	3.879	4.094	4.324	4.541	4.736	
Instron 2												
Rate: 5.08($\frac{\text{mm}}{\text{min}}$)												
E, J		.024	.122	.313	.613	1.024	1.545	2.177	2.898	3.692	4.559	
D ² /E		20.833	8.197	7.188	6.525	6.104	5.825	5.627	5.521	5.485	5.484	
Instron 3												
Rate: 25.4($\frac{\text{mm}}{\text{min}}$)												
E, J		.040	.181	.430	.787	1.252	1.826	2.497	3.238	4.047		
D ² /E		6.25	5.525	5.233	5.083	4.992	4.929	4.942	4.911	5.004		
Instron 4												
Rate: 1.27($\frac{\text{mm}}{\text{min}}$)												
E, J		.067	.270	.607	1.070	1.647	2.334	3.113	3.972	4.898	5.882	
D ² /E		3.731	3.704	3.707	3.738	3.795	3.856	3.935	4.025	4.157	4.250	
Instron 5												
Rate: 1.27($\frac{\text{mm}}{\text{min}}$)												
E, J		.127	.552	1.241	2.174	3.333	4.673					
D ² /E		1.969	1.812	1.813	1.840	1.875	1.926					
Instron 6												
Rate: 12.7($\frac{\text{mm}}{\text{min}}$)												
E, J		.322	.942	1.833	2.996	4.413						
D ² /E		.776	1.062	1.227	1.335	1.416						

TABLE 14 (con'd). QUASISTATIC PENETRATION TESTS ON SHALE

		P, Penetration Depth, mm										
		0.5	1.0	1.5	2.0	2.5	3.0	3.5	4.0	4.5	5.0	5.5
Instron 7												
Rate: 5.38($\frac{\text{mm}}{\text{min}}$)												
E, J		.152	.655	1.497	2.659	4.124	5.876	7.812	9.897	12.084	14.383	16.817
D ² /E		1.645	1.527	1.503	1.504	1.516	1.532	1.568	1.617	1.676	1.738	1.799
Instron 8												
Rate: 0.25($\frac{\text{mm}}{\text{min}}$)												
E, J		.186	.627	1.291	2.246	3.465	4.857	6.371				
D ² /E		1.344	1.595	1.743	1.781	1.804	1.853	1.923				
Instron 9												
Rate: 254($\frac{\text{mm}}{\text{min}}$)												
E, J		.108	.432	.972	1.727	2.699	3.887	5.290				
D ² /E		2.315	2.315	2.315	2.316	2.316	2.315	2.316				
Instron 10												
Rate: 50.8($\frac{\text{mm}}{\text{min}}$)												
E, J		.126	.495	1.095	1.912	2.934	4.135	5.490				
D ² /E		1.984	2.020	2.055	2.092	2.130	2.177	2.231				

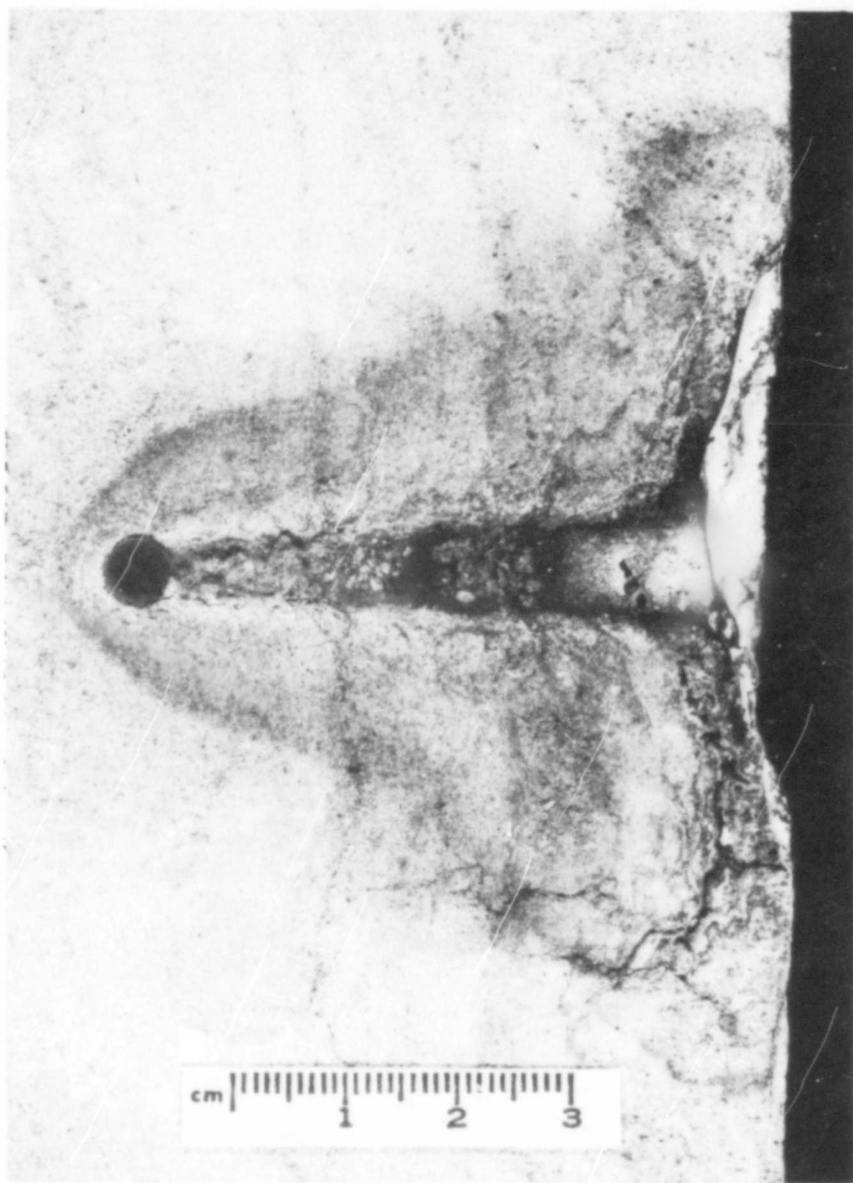


Fig. 19 Diametral Section of a $5\frac{1}{2}$ -in. D. x $5\frac{1}{2}$ -in. Shale Core, struck by a $\frac{1}{4}$ -in. Diameter Steel Sphere at a Velocity of 5300 ft/sec. Crater filled with a Catalyzed Methyl Methacrylate Glue Prior to Sectioning.

indentation in corresponding impact tests as might be expected. While in the initial range of penetration prior to a depth of one radius, there appears to be no obvious relationship between energy and penetration depth, a nearly linear equation seems to exist between these quantities beyond this domain.

d. Correlation of Penetration Data

An examination of the penetration phenomenon in shale at all impact velocities employed in the present study ranging from 51 to 2487 m/sec indicates that the viscous model is a reasonable approximation of the behavior pattern, whether the trajectory was normal or inclined to the target surface. The data from the rifled and unrifled projectiles fired from a tank gun are not included here due to sizable inconsistencies in penetration depths relative to the other results occasioned by tumbling that could not occur in the case of spherical projectiles. The curve of penetration depths vs. initial projectile momentum is presented in Figure 20 and indicates that a single line with a value $c = 29.5$ kg/sec is a good representation for all but the highest velocity tests, where three anomalies occur: the two shots with penetration depths greater than anticipated involved special experimental circumstances, one being a splitting of the sample and the other a back-up by a hard-steel cylinder. The highest impact velocity employed resulted in a penetration depth considerably smaller than expected on the basis of a linear representation as the result of projectile fragmentation. The initial projectile energy has been plotted against the square of the penetration depth, as shown in Figure 21; this diagram indicates that while a single line with constant $Q = 0.339 \text{ J/mm}^2$ approximates the entire span of the data, a better description of the experimental results is given by one line for the low-velocity tests and another for the higher velocity experiments, with values of $Q = 0.489 \text{ J/mm}^2$ and $Q = 0.284 \text{ J/mm}^2$, respectively. The overall pattern of the results agrees at least qualitatively with that of Reference [15].

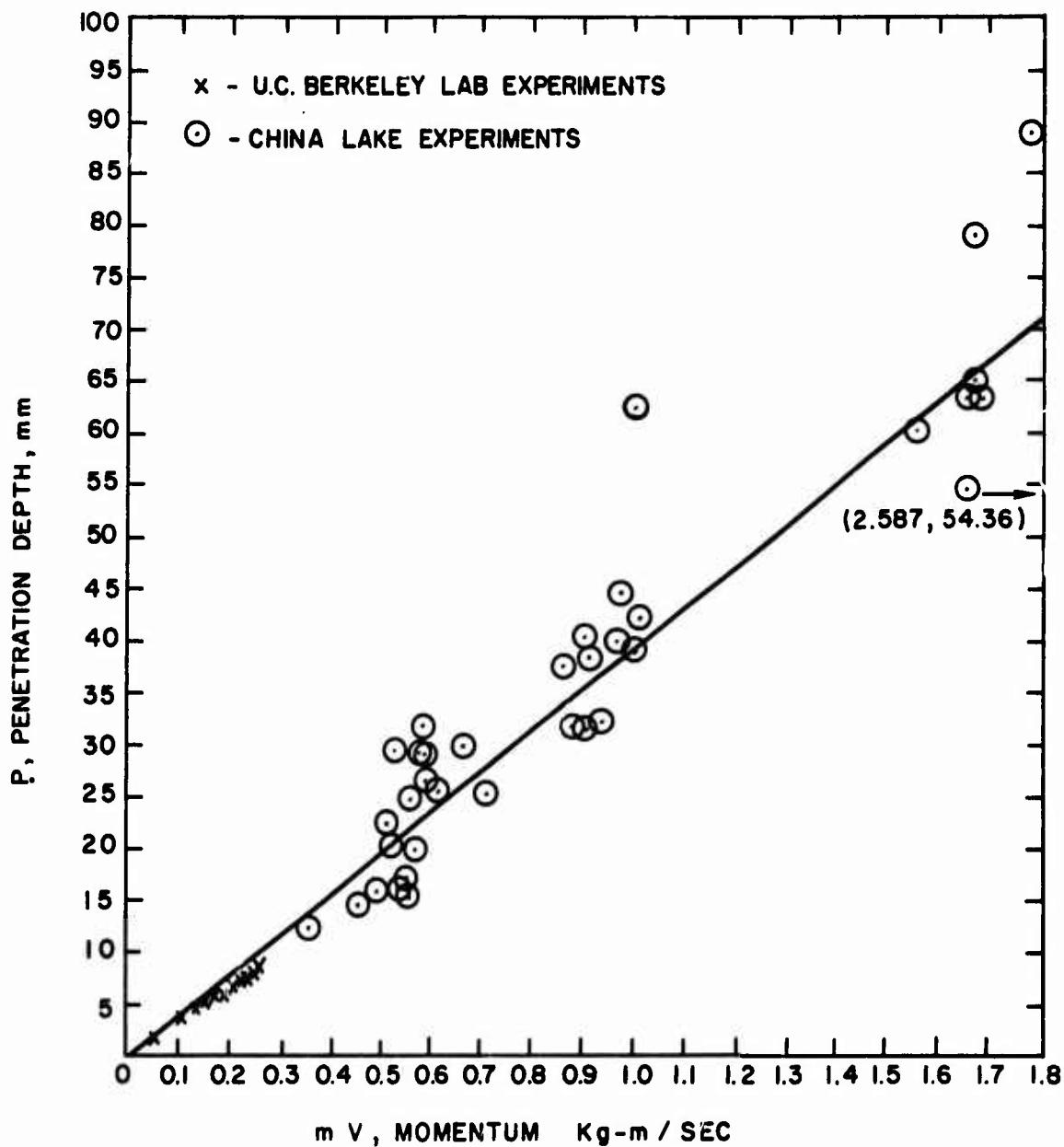


Fig. 20 - Penetration Depth as a Function of Initial Projectile Momentum

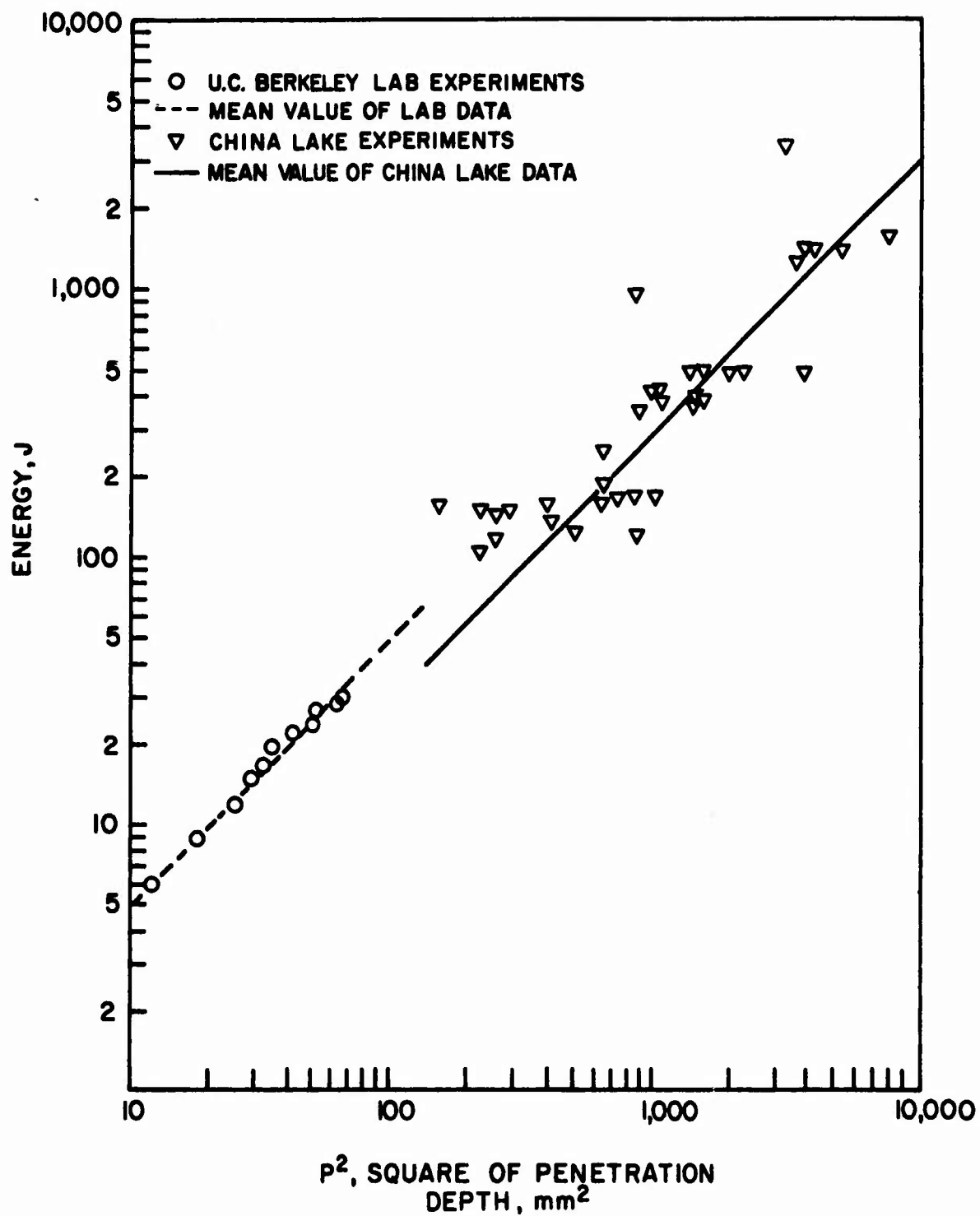


Fig. 21 - Square of Penetration Depth as a Function of the Initial Projectile Energy for Shale

SECTION V

SUMMARY

This document represents the final technical report for contract No. DNA001-73-C-0226 between the University of California, Berkeley and the Defense Nuclear Agency and, together with report DNA 3416Z, describes the accomplishments achieved during the two-year program of the project. The work consisted of laboratory investigations of the impact of a spherical steel projectile on disks of diorite and shale at velocities ranging from 51 to 1718 m/sec and a selected series of ordinance firings in the field. The field tests and higher velocity laboratory tests were performed by the personnel of the Naval Weapons Center, China Lake, and were described completely in Reference [8]. On the basis of the overall results, it is concluded that:

1. The comminution theories of Bond, Kick and Rittinger, designed for quasi-static crushing of brittle rock, are not directly applicable to projectile impact on a target modeled as a semi-infinite solid. Since the underlying assumption of these laws is that the basic shape of the particle remains unchanged, it is obvious that any process which leaves all but a relatively small percentage of the parent configuration completely intact falls outside the scope of these theories.

2. The particle size distribution obtained from the present comminution process in diorite appears to follow a normal logarithmic pattern permitting its description in terms of the mean and the standard deviation, somewhat analogous to what was found in crushing and grinding operations. Higher impact velocities produced smaller mean sizes of the ejecta.

3. The ballistic pendulum arrangement originally employed could be expediently replaced by a fixed test stand since the energy consumed in the swing was found to be a completely negligible fraction of the initial value.

4. Impact on different types of rock produced different shapes of the emitted ejecta. In the case of diorite, this formed a hollow cone whose kinetic energy was found to be about 10 percent of the initial value; in the case of limestone and shale, a rodlike emission was observed, but with a kinetic energy of only about 0.1 percent of the impinging striker.

5. The rebound velocity of the striker amounted to about 2 percent in the case of diorite and a negligible fraction in the case of the softer materials. Larger ejected fragments, initially separately examined, also failed to represent more than a vanishingly small portion of the available energy.

6. The energy propagated in the form of strain waves clustered around a value of about 10 percent of the original energy. The strain wave was the agent that produced additional cracks beyond those preexisting outside the domain of the crater; however, the area associated with these cracks could only be estimated in terms of upper and lower bounds.

7. The energy of comminution for the diorite samples was found to be in the range from 70 to 85 percent of the total.

8. Although enormous scatter was observed in the quasi-static experiments on shale, the dynamic tests at lower velocities conformed very well to a simple linearly viscous model that was also a reasonable approximation for the higher velocity regimes.

9. No permanent deformation of the projectiles was observed in any of the tests of the present program.

10. The ejecta surface area was computed on the basis of the measured crater mass and three assumed shapes of the ejecta characterized by a single dimensional parameter; these geometries were believed to be a reasonable approximation of the captured fragments based on their microscopic analysis.

The original proposal addressed itself to the examination of comminution in soft rocks by various experimental techniques that would provide separately information concerning the diverse phenomena involved in the overall process. Both shale and limestone samples were examined; however, when it was noted that comminution did not play a major role in the laboratory impact tests on soft rock, an expanded sequence of experiments was undertaken for the hard rock diorite at these speeds in order to study cases where ejecta formation appeared to be important. Nevertheless, in tests on shale involving a range of initial kinetic energies from 1.35 J to 3.65×10^6 J, the penetration depth scaled reasonably well with both initial momentum and initial energy. Particle size distributions have been obtained both in the lower and the

higher velocity regions and recapitulated in Reference [8]. Thus, results have been obtained in all areas stated in the proposal, and estimates of the energy required to produce unit new surface have been advanced.

It was originally indicated that the period of investigation was too short to permit a comprehensive analysis and modeling of the impact and comminution phenomenon and that the present investigation could serve at most as a point of departure for such an all-inclusive program, and this turned out to be the case. Severe experimental difficulties were encountered in the collection and sizing of all ejecta, whether at the lower or higher impact velocities. The determination of the new surfaces formed by the cracks generated by the passage of the transient produced by the impact could not be accomplished with any degree of accuracy or consistency; this is believed to be due to the inhomogeneous distribution of the preexisting microcracks. Finally, further information is needed for the construction of a proper mechanical model that will predict the microscopic phenomena involved in the cracking fracture and ejecta formation of hard rocks such as diorite. In the case of shale, where compaction appears to be an additional aspect of the contact problem, it is possible that, at least in the lower ranges of impact velocity, a simple model based on viscous considerations could be refined to provide adequate predictive capabilities.

LIST OF REFERENCES

1. v. Rittinger, P.R., Lehrbuch der Aufbereitungskunde. Berlin, 1867.
2. Kick, F., "Das Gesetz der proportionalen Widerstände und seine Anwendung," Dinglers Journal, 1883, pp. 141-145.
3. Bond, F. C., "The Third Theory of Comminution," Transactions of the American Institute of Mining Engineers, v. 193, 1952, pp. 484-494.
4. Walker, W. H., et al., Principles of Chemical Engineering. 3rd ed. New York, McGraw-Hill Book Company, 1937.
5. Beke, B., Principles of Comminution. Budapest, Akademiai Kiado, 1964.
6. Jowett, A., "An Introduction to the Assessment of Energy Requirements and Product Size in Comminution," Minerals Science and Engineering, v. 3, 1971, pp. 33-43.
7. Oka, Y., and Majima, H., "A theory of Size Reduction involving Fracture Mechanics," Canadian Metallurgical Quarterly, v. 9, 1970, pp. 429-439.
8. Goldsmith, W., "Fragmentation Processes in Soft Rock," Report DNA 3416Z, Defense Nuclear Agency, Washington, D.C., 1975. (See also Finnegan, S.A., and Goldsmith, W., "Projectile Impact on Shale," Naval Weapons Center, China Lake, California, Report NWC TP 5700, January 1975.)
9. Shockey, D. A., et al., "Development of a Capability for Predicting Cratering and Fragmentation Behavior in Rock," Report DNA 3730F, Defense Nuclear Agency, Washington, D.C., 1975.
10. Goldsmith, W., and Austin, C. F., "Some Dynamic Characteristics of Rocks," Stress Waves in Anelastic Solids, Proceedings of an International Symposium on Stress Waves in Anelastic Solids, W. Prager and H. Kolsky, eds. Berlin, J. Springer, 1964, pp. 275-303.
11. Ricketts, T. E., and Goldsmith, W., "Dynamic Properties of Rocks and Composite Structural Materials," International Journal of Rock Mechanics and Mineral Sciences, v. 7, 1970, pp. 315-335.
12. Goldsmith, W., and Lyman, P. T., "The Penetration of Hard-Steel Spheres into Plane Metal Surfaces," Journal of Applied Mechanics, v. 27, 1960, pp. 717-725.
13. Goldsmith, W., and Taylor, R. L., "Wave Traversal and Comminution of Rock," First Annual Report, NSF RANN Grant GI-39121, NTIS No. NSF-RA-T-74-042, University of California, Berkeley, June 15, 1974.
14. Goldsmith, W., and Allen W. A., "Graphical Representation of the Spherical Propagations of Explosive Pulses in Elastic Media," Journal of the Acoustical Society of America, v. 27, 1955, pp. 47-55.
15. Bauer, A., and Calder, P. N., "Projectile Penetration in Rock," Proceedings of 5th Canadian Rock Mechanics Symposium, December 1968, Toronto, Ontario, 1969, pp. 157-170.

Appendix A - Computer Program for Crack Surface Area Evaluation

```

PROGRAM CRACKS(INPUT,OUTPUT,TAPF5=INPUT,TAPF6=OUTPUT)
DIMENSION X1(300),X2(300),Y1(300),Y2(300),PHI(300),AREA(300)
+LINE(2),DATE(4),DEPTH(16)
REAL L(300)
DATA LATL(1,76)TEST D/DATE(2)/DATE /
C-----
C-----READ IN SAMPLE IDENTIFICATION, NUMBER OF CRACKS AND ENERGY*
C-----OF COMMUNICATION
C-----
READ(5,108) DATE(3), DATE(4), NCRACK,ENERGY
C-----
C-----READ IN CROSS-SECTIONAL CRACK DATA
C-----
READ(5,109) SPACE,(DEPTH(I),I=1,12),FACT
PI=3.1415926
TAREA=0.0
TL=0.0
DO 201 I=1,NCRACK
C-----
C-----READ IN CRACK DATA
C-----
READ(5,111) X1(I),Y1(I),X2(I),Y2(I)
C-----
C-----COMPUTE THE LENGTH, ANGLE WITH RESPECT TO THE AXIS OF
C-----SYMMETRY AND THE AREA ASSOCIATED WITH EACH CRACK
C-----
L(I)=SQRT((Y2(I)-Y1(I))*(Y2(I)-Y1(I))+(X2(I)-X1(I))*(X2(I)-X1(I)))
Y=Y2(I)-Y1(I)
X=X2(I)-X1(I)
PHI(I)=100.0
IF(Y.NE.0.0) PHI(I)=ATAN(X/Y)*180./PI
AREA(I)= PI*L(I)*(X1(I)+X2(I))
AREA(I)=ABS(AREA(I))
C-----
C-----COMPUTE THE TOTAL AREA AND TOTAL LENGTH OF ALL CRACKS
C-----
TAREA=TAREA+AREA(I)
TL=TL+L(I)
201 CONTINUE
WRITE(6,104)
WRITE(6,105) (DATE(I),I=1,4)

WRITE(6,107) NCRACK,TAREA,ENERGY
WRITE(6,106)
DO 202 I=1,NCRACK
WRITE(6,103) I,X1(I),Y1(I),X2(I),Y2(I),L(I),PHI(I),AREA(I)
202 CONTINUE
WRITE(6,104)
WRITE(6,112) TL
WRITE(6,104)

101 FORMAT(0F10.0)
103 FORMAT(20X,10,5F8.4,2F8.2)
104 FORMAT(11I1)
105 FORMAT(45X,'*CRACK ANALYSIS*.'/, 42X,4A6.'/)
106 FORMAT(20X,'*CRACK*+34X,*LENGTH ANGLE AREA*./,22X,*NUMBER X1(
+MM) Y1(MM) X2(MM) Y2(MM) (MM) (DEG) (SQ.MM)*./)
107 FORMAT(/+34X,*TOTAL CRACKS SEEN IN DIAMETRAL FACE = +.I3./+39X+
+*TOTAL AREA (SQ.MM.) = +F8.2/ +39X,*INPUT ENERGY (JOULES) = +
+F9.3./)
108 FORMAT(246,13,F5.1)
109 FORMAT(16F5.3)
110 FORMAT(1A,2A,TOTAL CRACK LENGTH = + F10.2)
STOP
END

```

DISTRIBUTION LIST

DEPARTMENT OF DEFENSE

Assistant to the Secretary of Defense
Atomic Energy
ATTN: Honorable Donald R. Cotter

Director
Defense Advanced Research Projects Agency
ATTN: NMRO
ATTN: PMO
ATTN: STO
ATTN: Tech. Lib.

Director
Defense Civil Preparedness Agency
ATTN: Tech. Lib.

Defense Documentation Center
12 cy ATTN: TC

Director
Defense Intelligence Agency
ATTN: DI-7D, Edward O' Farrell
ATTN: DI-7E

Director
Defense Nuclear Agency
ATTN: STSI, Archives
ATTN: DDST
2 cy ATTN: SPSS
2 cy ATTN: STTL, Tech. Lib.

Chairman
Dept. of Defense Explo. Safety Board
ATTN: DD/S&SS

Director of Defense Research & Engineering
ATTN: DD/S&SS
ATTN: AD/SW
ATTN: DD/TWP

Commander
Field Command
Defense Nuclear Agency
ATTN: FCPR

Director
Interservice Nuclear Weapons School
ATTN: Tech. Lib.

Director
Joint Strategic Target Planning Staff, JCS
ATTN: STINFO Library

Chief
Livermore Division, Field Command, DNA
Lawrence Livermore Laboratory
ATTN: FCPRL

Weapons Systems Evaluation Group
ATTN: Doc. Con.

DEPARTMENT OF THE ARMY

Dep. Chief of Staff for Research Dev. & Acq.
ATTN: Tech. Lib.

DEPARTMENT OF THE ARMY (Continued)

Director
Ballistic Missile Defense Advanced Technical Center
ATTN: CRDABH-S
ATTN: CRDABH-X

Chief of Engineers
Department of the Army
ATTN: DAEN-RDM
ATTN: DAEN-MCE-D

Deputy Chief of Staff for Ops. & Plans
ATTN: Tech. Lib.

Commander
Harry Diamond Laboratories
ATTN: AMXDO-TI, Tech. Lib.
ATTN: AMXDO-NP

Director
U. S. Army Ballistic Research Laboratories
ATTN: W. Taylor
ATTN: AMXBR-X, Julius J. Meszaros
ATTN: Tech. Lib., Edward Balcy
ATTN: J. H. Keefer

Commander
U. S. Army Engineer Center
ATTN: ATSEN-SY-L

Project Engineer
U. S. Army Engineer Division, Huntsville
ATTN: HNDSE-R, Michael M. Dembo

Division Engineer
U. S. Army Engineer Division, Ohio River
ATTN: Tech. Lib.

Director
U. S. Army Engineer Waterways Experiment Station
ATTN: Tech. Lib.
ATTN: Guy Jackson
ATTN: John N. Strange
ATTN: Leo Ingram
ATTN: William Flathau

Commander
U. S. Army Mat. & Mechanics Research Center
ATTN: Tech. Lib.

Commander
U. S. Army Materiel Dev. & Readiness Command
ATTN: Tech. Lib.
2 cy ATTN: AMCRD-WN
2 cy ATTN: AMCRD-BN

Commander
U. S. Army Missile Command
ATTN: Tech. Lib.

Commander
U. S. Army Nuclear Agency
ATTN: ATCA-NAW
ATTN: Tech. Lib.

DEPARTMENT OF THE NAVY

Chief of Naval Material
ATTN: Mat. 0323

Chief of Naval Operations
ATTN: OP-03EG
ATTN: OP-085F

Chief of Naval Research
ATTN: Code 464, Jacob L. Warner
ATTN: Nicholas Perrone
ATTN: Code 464, Thomas P. Quinn
ATTN: Tech. Lib.

Officer-in-Charge
Civil Engineering Laboratory
ATTN: Stan Takahashi
ATTN: Tech. Lib.
ATTN: R. J. Odello

Commander
Naval Electronic Systems Command
ATTN: PME 117-21A

Commander
Naval Facilities Engineering Command
ATTN: Code 03A
ATTN: Tech. Lib.
ATTN: Code 04B

Superintendent
Naval Postgraduate School
ATTN: Code 2124, Tech. Rpts. Librarian

Director
Naval Research Laboratory
ATTN: Code 2027, Tech. Lib.

Commander
Naval Surface Weapons Center
ATTN: Code WA-501, Navy Nuc. Prgms. Off.
ATTN: Code WX-21, Tech. Lib.

Commander
Naval Surface Weapons Center
ATTN: Tech. Lib.

President
Naval War College
ATTN: Tech. Lib.

Commanding Officer
Naval Weapons Evaluation Facility
ATTN: Tech. Lib.

Director
Strategic Systems Project Office
ATTN: NSP-43, Tech. Lib.

DEPARTMENT OF THE AIR FORCE

AF Geophysics Laboratory, AFSC
ATTN: LWW, Ker C. Thompson
ATTN: SUOL, AFICRL, Research Library

AF Institute of Technology, AU
ATTN: Library, AFIT, Bldg. 640, Area B

DEPARTMENT OF THE AIR FORCE (Continued)

AF Weapons Laboratory, AFSC
ATTN: Robert Port
ATTN: DEV, Jimmie L. Bratton
ATTN: DEV, M. A. Plamondon
ATTN: SUL

Headquarters
Air Force Systems Command
ATTN: DLCAW
ATTN: Tech. Lib.

Commander
Foreign Technology Division, AFSC
ATTN: TD-BTA, Library

HQ USAF/IN
ATTN: INATA

HQ USAF/PR
ATTN: PRE

HQ USAF/RD
ATTN: RDQPN

Commander
Rome Air Development Center, AFSC
ATTN: EMTLD, Doc. Lib.

SAMSO/MN
ATTN: MNN

Commander in Chief
Strategic Air Command
ATTN: NRI-STINFO Library

ENERGY RESEARCH & DEVELOPMENT ADMINISTRATION

University of California
Lawrence Livermore Laboratory
ATTN: Tech. Info., Dept. L-3
ATTN: Larry W. Woodruff, L-125

Los Alamos Scientific Laboratory
ATTN: Doc. Con. for Reports Lib.

Sandia Laboratories
Livermore Laboratory
ATTN: Doc. Con. for Tech. Lib.
ATTN: Doc. Con. for L. Hill

Sandia Laboratories
ATTN: Doc. Con. for 3141, Sandia Rpt. Coll.

U. S. Energy Research & Development Administration
Albuquerque Operations Office
ATTN: Doc. Con. for Tech. Lib.

U. S. Energy Research & Development Administration
Division of Headquarters Services
ATTN: Doc. Con. for Class. Tech. Lib.

U. S. Energy Research & Development Administration
Nevada Operations Office
ATTN: Doc. Con. for Tech. Lib.

Union Carbide Corporation
ATTN: Civil Def. Res. Proj.
ATTN: Doc. Con. for Tech. Lib.

OTHER GOVERNMENT AGENCIES

Bureau of Mines
ATTN: Tech. Lib.

Department of the Interior
Bureau of Mines
ATTN: Tech. Lib.

Department of the Interior
U.S. Geological Survey
ATTN: J. H. Healy
ATTN: Cecil B. Raleigh

DEPARTMENT OF DEFENSE CONTRACTORS

Aerospace Corporation
ATTN: Tech. Info. Services

Agabian Associates
ATTN: M. Agabian

Applied Theory, Inc.
2 cy ATTN: John G. Trulio

Avco Research & Systems Group
ATTN: Research Library, A-830, Rm. 7201

Battelle Memorial Institute
ATTN: Tech. Lib.

The BDM Corporation
ATTN: Tech. Lib.

The Boeing Company
ATTN: Aerospace Library

California Research & Technology, Inc.
ATTN: Ken Kreyenhagen
ATTN: Tech. Lib.

University of California
ATTN: G. Sackman
50 cy ATTN: W. Goldsmith

Calspan Corporation
ATTN: Tech. Lib.

Civil/Nuclear Systems Corporation
ATTN: Robert Crawford

University of Dayton
ATTN: Hallock F. Swift

University of Denver
Colorado Seminary
ATTN: Sec. Officer for Tech. Lib.
ATTN: Sec. Officer for J. Wisotski

EG&G, Inc.
Albuquerque Division
ATTN: Tech. Lib.

General American Transportation Corporation
ATTN: G. L. Neidhardt

General Electric Company
TEMPO-Center for Advanced Studies
ATTN: DASIAC

DEPARTMENT OF DEFENSE CONTRACTORS (Continued)

IIT Research Institute
ATTN: Milton R. Johnson
ATTN: R. E. Welch
ATTN: Tech. Lib.

Institute for Defense Analyses
ATTN: IDA, Librarian, Ruth S. Smith

Kaman Avidyne
Division of Kaman Sciences Corporation
ATTN: E. S. Criscione
ATTN: Norman P. Hobbs
ATTN: Tech. Lib.

Kaman Sciences Corporation
ATTN: Library

Lockheed Missiles & Space Company
ATTN: Tom Geers, Dept. 52-33, Bldg. 205
ATTN: Tech. Info. Ctr., D/Coll.

Lovelace Foundation for Medical Education
ATTN: Asst. Dir. of Res., Robert K. Jones
ATTN: Tech. Lib.

McDonnell Douglas Corporation
ATTN: Robert W. Halprin

Merritt Cases, Incorporated
ATTN: J. L. Merritt
ATTN: Tech. Lib.

The Mitre Corporation
ATTN: Library

Nathan M. Newmark
Consulting Engineering Services
ATTN: Nathan M. Newmark

Physics International Company
ATTN: Doc. Con. for Larry A. Behrmann
ATTN: Doc. Con. for Tech. Lib.
ATTN: Doc. Con. for Dennis Orphal
ATTN: Doc. Con. for Robert Swift
ATTN: Doc. Con. for E. T. Moore
ATTN: Doc. Con. for Charles Godfrey
ATTN: Doc. Con. for Fred M. Sauer

R & D Associates
ATTN: William B. Wright, Jr.
ATTN: Jerry Carpenter
ATTN: J. G. Lewis
ATTN: Tech. Lib.
ATTN: Albert L. Latter
ATTN: Sheldon Schuster
ATTN: Henry Cooper
ATTN: Harold L. Brode
ATTN: Bruce Hartenbaum

Science Applications, Inc.
ATTN: D. E. Maxwell
ATTN: David Bernstein

Science Applications, Inc.
ATTN: R. Seebaugh
ATTN: John Mansfield

DEPARTMENT OF DEFENSE CONTRACTORS (Continued)

Science Applications, Inc.

ATTN: Tech. Lib.

ATTN: Michael McKay

Science Applications, Inc.

ATTN: R. A. Shunk

Shock Hydrodynamics, Inc.

A Div. of Whittaker Corporation

ATTN: L. Zernow

Southwest Research Institute

ATTN: A. B. Wenzel

ATTN: Wilfred E. Baker

Stanford Research Institute

ATTN: Carl Petersen

ATTN: George R. Abrahamson

ATTN: Burt R. Gasten

Systems, Science & Software, Inc.

ATTN: Robert T. Allen

ATTN: Donald R. Grine

ATTN: Tech. Lib.

ATTN: Ted Cherry

ATTN: Thomas D. Riney

Terra Tek, Inc.

ATTN: Sidney Green

ATTN: Tech. Lib.

Tetra Tech, Inc.

ATTN: Li-San Hwang

ATTN: Tech. Lib.

TRW Systems Group

ATTN: Benjamin Sussholtz

ATTN: Paul Lieberman

ATTN: William Rowan

ATTN: Norm Lipner

ATTN: Tech. Info. Ctr., S-1930

ATTN: Pravin Bhutta

ATTN: Jack Farrell

DEPARTMENT OF DEFENSE CONTRACTORS (Continued)

TRW Systems Group

San Bernardino Operations

ATTN: Greg Hulcher

Universal Analytics, Inc.

ATTN: E. J. Field

The Eric H. Warg

Civil Engineering Research Facility

ATTN: Neal Baum

ATTN: Larry Bickle

Washington State University

Administrative Office

ATTN: Arthur Miles Hohorf for George Duval

Weidlinger Assoc. Consulting Engineers

ATTN: Melvin L. Baron

Weidlinger Assoc. Consulting Engineers

ATTN: J. Isenberg

Westinghouse Electric Company

Marine Division

ATTN: W. A. Volz